# Design and Implementation of an Unstable Resonator for a Large Bore Multi-kilowatt $CO_2$ Laser

Thesis

Submitted To

Graduate Engineering and Research

School of Engineering

## University of Dayton

In Partial Fulfillment of the Requirements for

The Degree

Master of Science in Electro-Optics

by

George Logan DesAutels

University Of Dayton

Dayton, Ohio

December 1998

Design and Implementation of an Unstable Resonator for a Large Bore Multi-kilowatt $CO_2$ Laser

APPROVED BY:

Perry P. Yaney, Ph.D
Advisory Committee Chair
Professor, Electro-Optics

Leno M. Pedrotti, Ph.D.
Committee Member
Professor, Electro-Optics

Michael L. Lander
Committee Member
LHMEL Facility Program Manager
Electro-Optics Engineer

Donald L. Moon, Ph.D.
Associate Dean
Graduate Engineering Programs and Research
School of Engineering

Blake Cherrington, Ph.D., P.E.
Dean, School of Engineering

# ABSTRACT

Design and Implementation of an Unstable Resonator for a Large Bore Multi-kilowatt $CO_2$ Laser System

Name: DesAutels, George, Logan
University of Dayton

Advisor: Dr. Perry P. Yaney

The Laser Hardening Materials Evaluation Laboratory (LHMEL) facility located at Wright Patterson Air Force Base requisitioned for the design of an unstable resonator for their 15-kilowatt research laser system (LHMEL I-R). The requirements were high output power, good mode discrimination and a small focused spot diameter. The applications of this resonator will be for materials testing/evaluation, cutting and welding. A number of designs were investigated for the LHMEL facility's 15-kilowatt research laser system. This laser system also had to be evaluated to determine the gain characteristics of the laser medium. After a design was chosen, the new resonator was tested and characterized. An unobscured unstable resonator was implemented on LHMEL I-R. This design has the capability of producing the above requirements. One limiting factor was overlooked in this design; that is, the unstable resonator utilizes all 4-inches of the laser cavity. This creates a problem when aligning the resonator, because the optics has to be perfectly aligned to avoid interference with the laser cavity walls, which distorts the laser beam. Therefore, to resolve this alignment difficulty, a hard aperture was designed

to limit the size of the beam inside the laser resonator. This essentially made the cavity walls larger with respect to the internal laser beam, which made aligning the optics, much easier and improved the quality of the output beam. However, a larger hard aperture is needed, the first aperture design *helped* but was not quite sufficient, the output beam is still being distorted from the beam interfering with the cavity walls. Since the beam inside the resonator is nevertheless being distorted, more transverse modes are actively running than predicted. As a result, the focused spot size and output power was not measured to the expected values. However, once a new (larger) hard aperture is implemented the results are expected to be closer to the predicted values.

# ACKNOWEDGEMENTS

I would foremost like to my wife Kristen for all of her encouragement, motivation and support. I would secondly like to thank my parents for instilling in me to believe that I could achieve anything, and that nothing was ever out of my reach. Thanks also to Mike Lander, John Bagford, Dan Norris, Charlie O'blinger, Marsha Wolf, Keith Maxwell, Dan Daniels, Greg King and Pete Hall for their assistance during my research. In addition, I want to thank Mike Lander and the Anteon Corporatin for the financial assistance. A special thanks is due to Chris Brewer, Andy Zakel and Leo Gonzalez who consistently answered any of my questions. Thanks to Dr. Leno Pedrotti, for his encouragement and for being an excellent teacher. Finally, but not least, thanks to my advisor Dr. Perry Yaney who has been continually patient with me and for his guidance during this past year.

# TABLE OF CONTENTS

Chapter

Appendix

# LIST OF FIGURES

## LIST OF TABLES

The current stable resonator design is comprised of a rear concave copper mirror and a flat ZnSe partially reflective (75%) output coupler. This configuration is beneficial because it utilizes most of the volume of the gain medium, which permits maximum power extraction. The rear reflector is nearly flat (radius of curvature of 35 m), the front coupler is flat, and the cavity length is 3.5 m. This configuration, however, does support multi-transverse mode operation, which produces the "flat top" intensity profile. While the "flat top" profile is valuable for some testing scenarios, its inability to be focused to a small spot is a detriment to other testing requirements. The idea of designing a cavity that would utilize most of the gain medium and produce a Gaussian profile was proposed. This would allow high output powers to be focused to a small spot.

This proposal led to the design and implementations of an unstable resonator for the LHMEL facility's 15-kW $CO_2$ large-bore laser system (LHMEL I-R). Unstable resonators are typically used in large-bore, high-powered laser systems because they utilize extensive volumes of the gain medium by spreading the light inside the laser cavity over most of the volume. The light tends to "walk out" of the cavity and exit out around the front coupler, which is generally a small mirror. The intensity distribution becomes a doughnut-shaped beam that has an intensity minimum in the near field, which smoothes out in the far field region giving a more uniform energy distribution. On the other hand, stable resonators that produce Gaussian beams accomplish this by constraining the light along the laser axis unlike the LHMEL facility's stable resonator, which uses most of the volume. The beam typically has an intensity peak at the center and a Gaussian intensity profile about the axis. Stable resonators are thus commonly used with low-gain small-bore laser systems.

In order to design a laser resonator that possesses the ability to extract high output power and to generate a Gaussian transverse intensity distribution, it was necessary to characterize the LHMEL I-R laser gain medium. Chapter 2 reviews the laser theory needed for this work. Two studies, discussed in Chapter 3, were performed to measure the small signal gain coefficient, $\gamma_o$, and the saturation intensity, $I_{s,}$ which are critical in determining the performance of a given laser device. Chapters 4 and 5 discuss various design issues and a selection of cavity designs that are suitable for LHMEL I-R laser. Chapter 6 presents the implementation of the chosen design, and in addition, contains a summary and proposals for future enhancements of the chosen design.

# CHAPTER 2

## Theory

### 2.1 Basic Laser Theory

Three fundamental elements are required to constitute a laser device: 1) A gain medium which can consist of one or more species of atoms, molecules or ions; 2) A pumping mechanism (often an electrical discharge) which transfers energy into the gain medium and excites the active species into high energy levels; 3) An optical resonator that permits the photons generated by the excited gain medium to make multiple passes through the amplifying gain medium by the use of two or more mirrors.

An excited medium can either emit photons spontaneously or by stimulation due to incident photons. Spontaneous emission transpires naturally due to the excited species dropping to a lower energy level without any external intervention. Stimulated emission occurs when an atom decays and releases its energy $h\nu$ upon interacting with a stimulating photon present in the field. Stimulated emission adds a photon to the field at the same frequency, polarization, and direction of travel and phase as the stimulating wave or photon.[1] Therefore, the first few spontaneously emitted photons can trigger stimulated emission of others, leading to a cascade of stimulated emission.[2] Figure 1 illustrates this process.

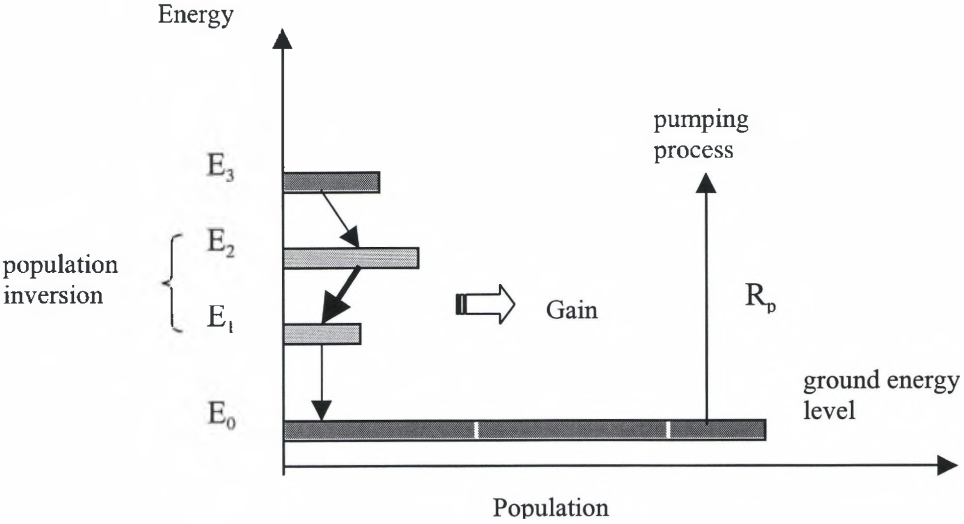

**Figure 2.1**. A typical population distribution for a four-level laser medium.

In Figure 2.1 the lowest or ground energy level, $E_0$, represents the state at which the majority of atoms and molecules reside at room temperature in the absence of any applied excitation. For convenience, 4-level atoms will be assumed. A pumping mechanism with a pumping rate of $R_p$ (atoms/cm$^{-3}$ s$^{-1}$) pumps a small portion of the atoms in $E_0$ into the upper levels (which may consist of many levels), or level $E_3$ for simplicity. Eventually, the atoms relax down from the pump level $E_3$ to the laser level $E_2$ at a rate defined as $\gamma_{32}$. It is here, between levels $E_2$ and $E_1$, that a population inversion is produced provided that the decay rate, $\gamma_{21}$, for an atom decaying between levels $E_2$ to $E_1$ is considerably smaller than the decay rate, $\gamma_{10}$. Thus, when the atoms are excited to $E_3$ they immediately drop to $E_2$ where they accumulate assuming $\gamma_{32} >> \gamma_{21}$. With the atoms accumulated in level $E_2$ giving population inversion, the cascading stimulated emission events between $E_2$ and $E_1$ produce optical gain. In the case of a molecular laser system, the transitions are between rotational-vibrational levels which enables the molecules to release their energy in the form of thermal photons. As the stimulated photons are emitted, the atoms or molecules continue to drop down the quantum energy level ladder until they reach the ground state.

The atoms that are going through the pumping and relaxation processes can be described mathematically by a set of rate equations. Using Figure 2.1, the equations for the four energy levels can be written as

$$\frac{dN_3}{dt} = R_p(N_0 - N_3) + N_3(-\gamma_{32} - \gamma_{31} - \gamma_{30}), \tag{2. 1}$$

$$\frac{dN_2}{dt} = \gamma_{32}N_3 - \frac{\sigma I_\nu}{h\nu}(N_2 - N_1) + N_2(-\gamma_{21} - \gamma_{20}), \tag{2. 2}$$

$$\frac{dN_1}{dt} = \gamma_{31}N_3 + \gamma_{21}N_2 + \frac{\sigma I_\nu}{h\nu}(N_2 - N_1) - \gamma_{10}N_1, \tag{2. 3}$$

$$\frac{dN_0}{dt} = \gamma_{30}N_3 + \gamma_{20}N_2 + \gamma_{10}N_1 - R_p(N_0 - N_3), \tag{2. 4}$$

where $N_i$ are the number densities in the states given by i = 0, 1, 2, 3, …n, $I_\nu$ is the flux at frequency $\nu = (E_2 - E_1)/h$, h is Planck's constant and $\sigma$ is the stimulated cross-section. These equations portray the rate of change in the number density of atoms in each level. Therefore, Equation 2.1 describes the upward pumping process, $R_p$, from the ground level, $E_0$, to the pump level, $E_3$. In Equations 2.2 and 2.3 the term, $\frac{\sigma I_\nu}{h\nu}$, represents the absorption and *stimulated emission* of photons by atoms in levels $E_2$ and $E_1$.

Once a population inversion is obtained, the medium exhibits gain and, with feedback provided by mirrors, oscillation can occur. The gain medium is characterized by the gain coefficient, $\gamma$, which is the fractional change in intensity of a light beam per unit length as it propagates through the medium. Some values of gain coefficients in different laser gain media are[3]

| Laser | Gain Medium | $\gamma$ – cm$^{-1}$ |
|---|---|---|
| Dye lasers | Chemical – Liquid | ~4 |
| Semiconductor lasers | Electronic – Solid | ~40 |
| Ar-Ion lasers | Electronic – Gas | ~0.03 |
| HeNe lasers | Electronic – Gas | ~0.001 |
| $CO_2$ lasers | Molecular – Gas | ~0.01 |

The gain coefficient for small values of intensity, $I_\nu$, in the laser medium is called the small signal gain coefficient $\gamma_o$. As the intensity increases, due to increasing number of stimulated emission events, the atoms in the upper laser energy level will decay to the lower laser level. This process progressively reduces population inversion thereby reducing the gain coefficient below $\gamma_o$. This process is called gain saturation. The threshold for lasing is achieved when the small signal gain coefficient, $\gamma_o$, equals the total effective loss coefficient of the cavity.

The gain coefficient, $\gamma$, of a laser medium in the z-direction is defined in the equation below

$$\frac{1}{I_\nu}\frac{dI_\nu}{dz} = \gamma(I_\nu) \quad , \qquad (2.5)$$

where $\gamma$ is a function of $I_\nu$, in general. The $CO_2$ gain medium studied here was operated in the homogeneous broadening regime (see Appendix D). For a homogeneous gain medium, $\gamma(I_\nu)$ is given by

$$\gamma(I_\nu)=\frac{\gamma_o}{1+g(\nu)\frac{I_\nu}{I_s}}, \qquad (2.6)$$

where g(ν) is the peak-normalized line shape function (g(ν)=1 at line center), and $I_s$ is the saturation intensity. The full expression for saturation intensity is derived in many laser physics books; however, a useful approximate form is given by

$$I_s=\frac{h\nu_o}{\sigma(\nu_o)\tau_2}, \qquad (2.7)$$

where $\nu_o$ is the frequency at the center of the laser line, $\sigma(\nu_o)$ is the cross section for stimulated emission at $\nu_o$ and $\tau_2$ is the lifetime of the upper laser level. The $CO_2$ laser involves as many as 200 vibration-rotational transitions in the 8 to 18 μm wavelength-range. The output of the LHMEL I-R laser is largely in the 9 to 10 μm range. Because of the complexity of the laser spectrum, only measured values of $I_s$ will be used. Therefore, the approach described in Chapter 3 was to measure $\gamma_o$ and $I_s$ and to use these values to predict the performance of the unstable resonator design.

Once the small signal gain coefficient and saturation intensity are known, the laser output power can be predicted. Using the Rigrod analysis[4] (see Appendix A ), the output intensity, $I_{out}$, can be calculated, which, with the area of the output beam, determines the output power. Equation (2.8) is the expression for the average output intensity using the Rigrod analysis

$$\frac{I_{out}}{I_s}=\frac{t_b t_2\left[\gamma_o l_g-\frac{1}{2}\ln\left(\frac{1}{t_a{}^2 t_b{}^2 r_1 r_2}\right)\right]}{\left(1-\sqrt{t_a{}^2 t_b{}^2 r_1 r_2}\right)\left(1+\sqrt{\frac{r_2 t_b{}^2}{r_1 t_a{}^2}}\right)}, \qquad (2.8)$$

where $r_1$ is the reflectance of the back mirror, $r_2$ is the reflectance of the front coupler, $l_g$ is the length of the laser gain medium and $t_2$ is the transmittance or output light coupling through the output mirror. Since the gas is in direct contact with the mirrored surfaces, there are no internal windows, which gives $t_a = t_b = 1$. This equation was used to find the output coupling that produces maximum output power for a given resonator design and gain medium characteristics.

## 2.2 Optical Resonators, Beam Quality and Modes

Laser oscillation can occur when the stimulated emission resonates along one axis (optical axis) by mirrors separated by a distance of many times the laser wavelength. There are different types of resonators used to shape the output beam's transverse pattern. Some of these include.[5]

Concave-convex resonator: A concave spherical mirror and a smaller diameter convex mirror separated by the difference of their focal lengths.

Confocal resonator: Two identically curved spherical mirrors separated by twice their focal length, which brings their focal points into coincidence.

Hemiconfocal resonator: A spherical mirror separated from a flat mirror by its focal length.

Hemispherical resonator: A spherical mirror separated from a flat mirror by its radius of curvature.

Plane-parallel resonator: Two flat mirrors separated by integral number, n, of half-wavelengths, λ/2.

There are two classes of laser resonators, stable and unstable. A resonator is said to be stable if a light ray initially parallel to the optical axis, but displaced from axis, could be reflected forever (if there are no losses) back and forth between the mirrors without escaping. There are also special cases of *marginal stability*. An example of this is the plane-parallel resonator. For this case, an initial light ray will oscillate forever as long as the mirrors are exactly parallel to each other. If these mirrors are not exactly parallel, then the light ray will "walk out" of the cavity around the mirrors. Selected resonator examples are shown in Figure 2.2.

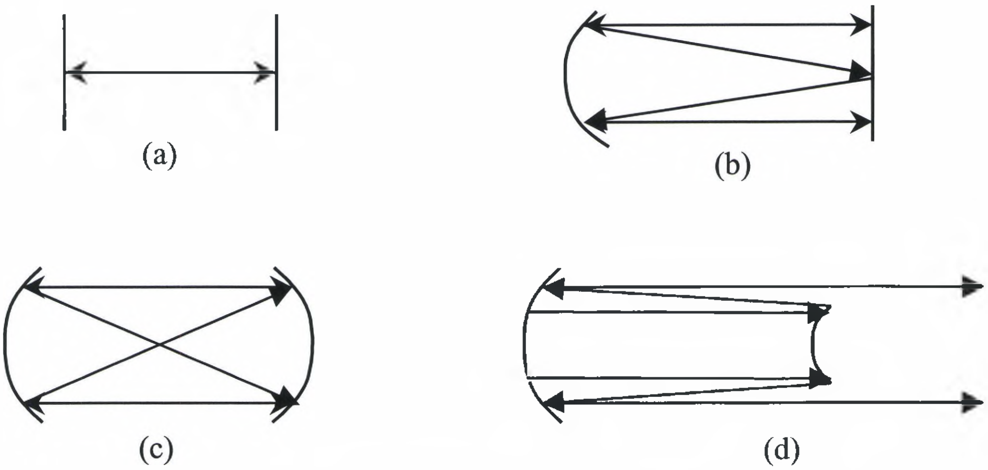

**Figure 2.2.** Examples of selected laser resonator designs. (a) Plane-parallel resonator (marginally stable). (b) Hemiconfocal resonator (stable). (c) Confocal resonator (stable). (d) Confocal-convex resonator (unstable).

In an unstable resonator similar to Figure 2.2(d), however, the mirrors are designed to allow the light rays to "walk out" of the cavity around the front mirror. This permits a larger volume of the laser gain medium to be used thereby extracting more output power (often used in high power laser systems). In most cases, the output beam has an annular profile with peak intensity in a ring around the axis, but with a minimum on axis. This is in contrast to a stable resonator which concentrates the light along the axis producing an intensity peak on the center line with a Gaussian intensity profile in the radial direction.

Optical resonators have two distinct types of modes: longitudinal and transverse. Figure 2.3 illustrates longitudinal modes, also known as axial cavity modes.[6]

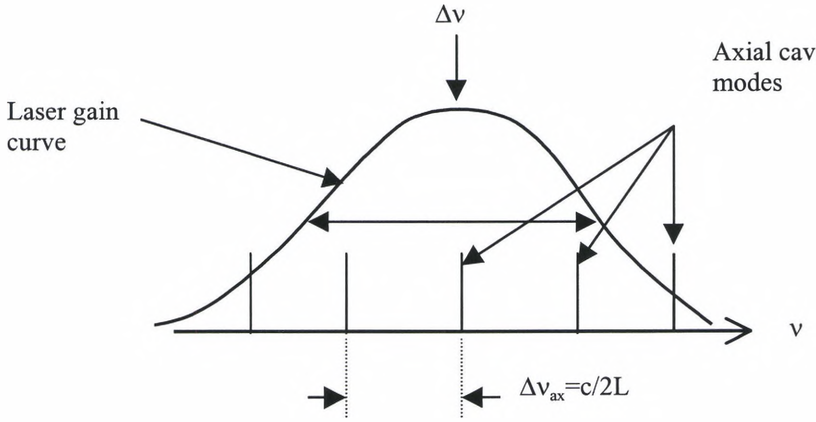

**Figure 2.3.** Multiple axial-mode frequencies under the atomic gain profile in a typical laser system. Where $\Delta\nu_{ax}$ is the evenly spaced axial-mode separation, c is the speed of light and L is the cavity length.

The axial modes of a laser cavity represent a set of frequencies under the laser gain curve, which are equally spaced by $\Delta\nu_{ax}$ (Hz). A laser can oscillate on just the centermost axial mode (homogeneous broadening) or on multiple axial modes simultaneously (inhomogeneous broadening). Larger, high-powered laser systems, like LHMEL I-R, typically are more likely to oscillate in multiple longitudinal (axial) modes due to multiple lasing frequencies of the medium. In some laser systems, however, it may be possible to oscillate in only a *single* centermost longitudinal mode if the cavity length, L, is short enough (c/2L) so that axial-mode spacing becomes larger the transition linewidth (laser gain curve), Δν. Usually the linewidth is much larger than the longitudinal mode spacing, thus, there will be several longitudinal-mode cavity resonances within the laser gain curve. In most (but not all) laser systems, controlling the longitudinal modes so that only a single centermost mode oscillates is less important than controlling the transverse modes, which determines the beam character.

For any type of laser cavity with mirrors, a discrete set of transverse modes will be produced within the cavity as the beam propagates between the mirrors. Transverse modes are the distinct amplitude and phase patterns that are self-reproducing as the wave propagates between the two mirrors of the optical resonator. These transverse modes are thus dependent on the specific curvature and shape of the cavity mirrors. Diffraction effects, caused by finite apertures within the laser cavity or off-axis propagation that acquires sufficient gain from the laser medium to overcome any losses, will cause these transverse modes to experience specific amounts of amplitude reduction and phase distortion for each mode. If any one of these modes can maintain a round-trip gain that exceeds the losses of the laser cavity, then it will be present in the beam profile.

Different types of optical cavities (planar, stable and unstable) will produce a specific type of beam profile, which is again dependent on the cavity mirrors and the diffraction effects caused by the finite apertures (mirrors) within the laser cavity. LHMEL I-R employed a stable resonator before the new unstable design was implemented, which produced a multi-TEM-mode "flat-top" output beam profile; therefore, the following paragraphs discuss the beam profiles and transverse modes produced by stable and unstable resonators.

Stable resonators typically produce the lowest-order transverse mode pattern, in which the diffraction losses are *very* small. The lowest and higher-order modes *very closely* resemble Hermite-Gaussian functions, which will not be discussed in this thesis but are described in many laser physics books.[6] Figure 2.4 below illustrates the first three Hermite-Gaussian modes for a diffraction limited stable cavity.

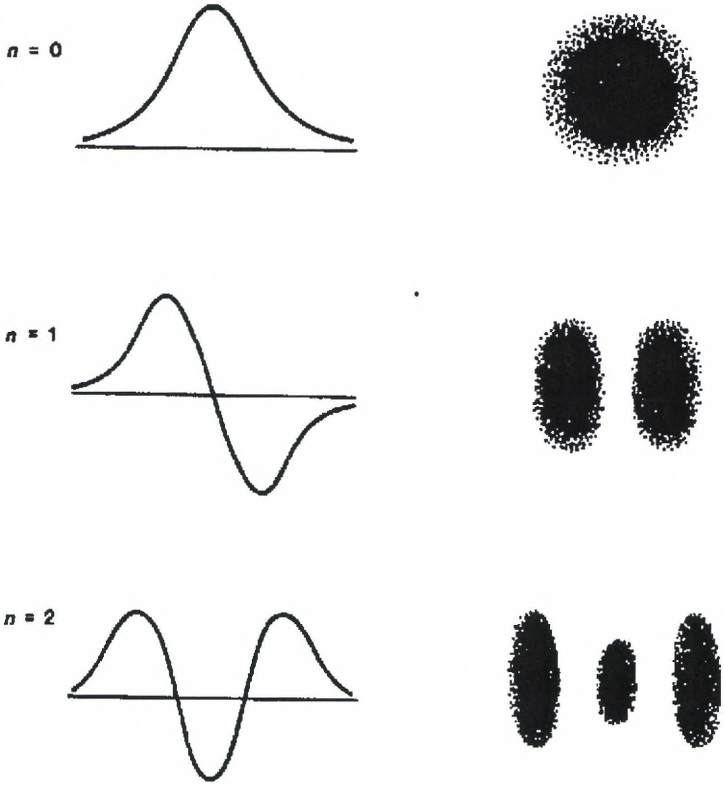

**Figure 2.4**. Hermite-Gaussian transverse-mode field and intensity patterns produced by a stable resonator [from Reference No. 6].

LHMEL I-R has a cavity with large diameter-to-length ratio , which primarily causes more diffraction affects thus creating a multi-TEM-mode “flat-top” output beam pattern represented in Figure 2.5.

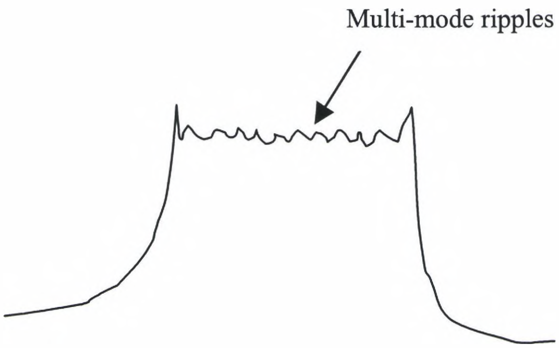

**Figure 2.5.** LHMEL I-R's multi-mode "flat-top" output beam pattern.

A typical unstable resonator, unlike stable resonators, has a diverging wavefront in the medium, which produces transverse mode patterns that use much more of the laser gain medium volume so as to extract higher output energies.[6] A typical unstable resonator, shown in Figure 2.6 below, has a "doughnut" shaped output beam pattern since the output coupler consists of a convex mirror smaller than the beam coming from the concave mirror.

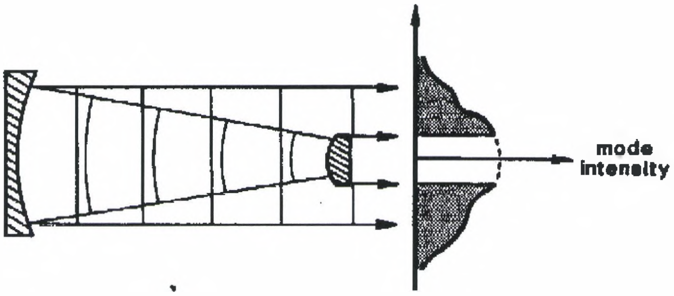

**Figure 2.6.** A typical unstable resonator transverse-mode profile [from Reference No. 6].

The design goal of this thesis was to utilize the unstable resonator's characteristic of extracting maximum energy from a large-volume laser gain medium while producing a near-Gaussian beam profile in the far-field.

Diffraction effects are more prominent in typical unstable resonators because the beam is the same size or larger than the mirrors, whereas, for stable resonators the diffraction effects, from the mirror edges, are minimal since the beam is much smaller than the mirrors. Diffraction in an unstable resonator in the near field (or close to the output coupler) are known as Fresnel diffraction. The output transverse mode pattern will oscillate periodically from zero to maximum with longitudinal position, and successive Fresnel zones will be observed.[6] The Fresnel number, N, gives the number of Fresnel zones by

$$N = \left( \frac{a_2^{\ 2}}{\lambda L} \right), \qquad (2.\ 9)$$

where $a_2$ is the radius of the output coupler (small front mirror in Figure 2.6) and L is again the length of the cavity. An equivalent Fresnel number, $N_{eq}$, can be defined for an unstable confocal (both mirrors having a common focal point) resonator by

$$N_{eq} = \frac{N}{2(M-1)}, \qquad (2.\ 10)$$

where M is the magnification. The equivalent Fresnel number is equal to the additional path length in half-wavelengths that a ray would travel from the edge of an output coupler, $m_2$, to the back mirror as compared to a ray going from the center of the same coupler to the back mirror, $m_1$. Figure 2.7 illustrates the meaning of the equivalent Fresnel number.

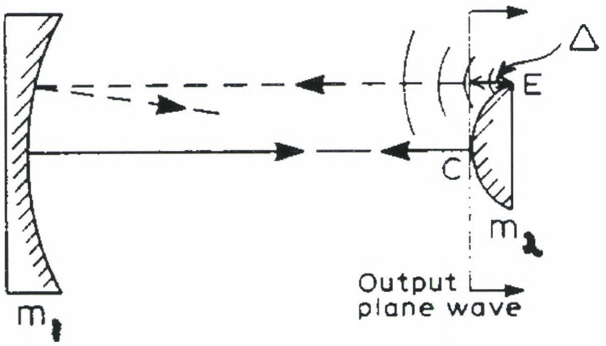

**Figure 2.7**. Illustrating the effect of edge diffraction for a confocal unstable resonator [from Reference No. 7].

Referring to Figure 2.7, for a sharp-edged output mirror there will be a narrow zone near the periphery of $m_2$ where the light is diffracted. Thus, while the majority of the wavefront is returned as a divergent beam to be re-collimated by $m_1$, a fraction of the edge-scattered wave can propagate back into the resonator. This edge-diffracted radiation, shown as a dashed line, converges back from $m_1$ towards $m_2$.[7] The extra distance that the edge-diffracted wave travels, compared to the plane wave reflected from the center of $m_2$ is Δ. Thus, Δ is defined as[7]

$$\Delta = \frac{N_{eq}\lambda}{2} \quad . \tag{2. 11}$$

For integral values of $N_{eq}$, the wavefront going towards $m_2$ is in phase with the edge-diffracted wavefront, therefore, can amplify the wavefront and increase the loss. When $N_{eq}$ is half-integral these waves are out of phase and the loss is reduced.

Fox and Li first calculated diffraction losses for unstable resonators.[6] These calculations are complicated and not shown here, but the results are shown in Figures 2.8 and 2.9.

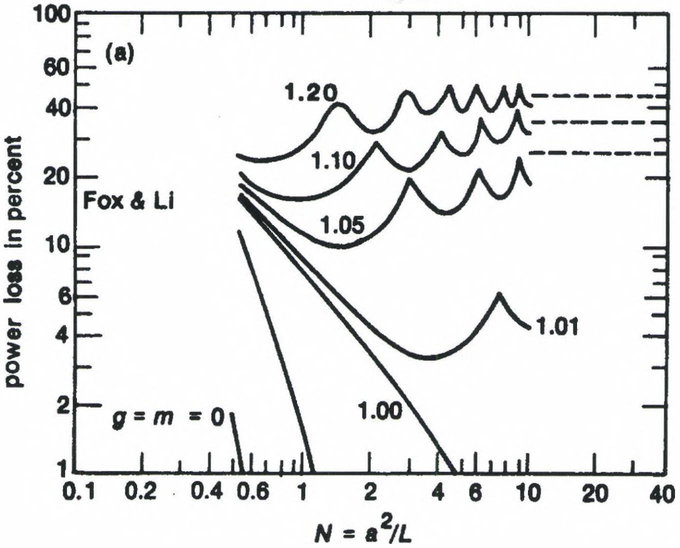

**Figure 2.8.** Power loss in percent verses Fresnel number for a symmetric strip unstable resonator, where g = 1 - (L/R) [from Reference No. 6].

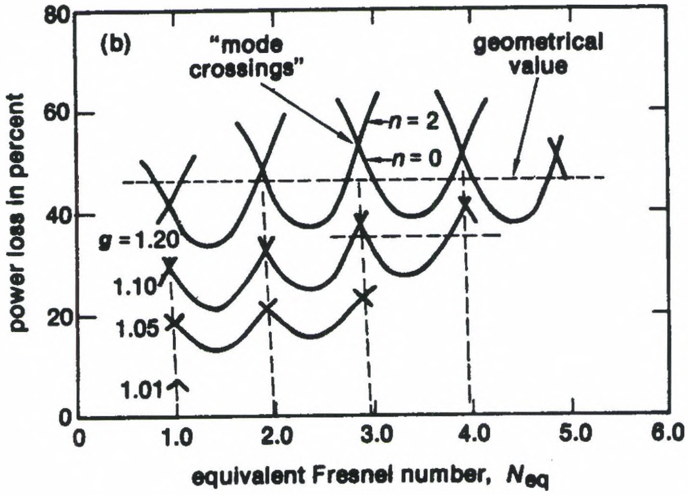

**Figure 2.9.** Power loss in percent verses the equivalent Fresnel number for a symmetric strip unstable resonator [from Reference No. 6].

Figure 2.8 shows a plot of the loss per bounce verses Fresnel number. Figure 2.9 repeats these calculations done by Fox and Li, but plotted against the equivalent Fresnel number.

Fox and Li noticed that when a resonator's g-parameter was in the stable region, the diffraction losses decreased with increasing Fresnel number. However, when the g-parameter fell in the unstable region, the diffraction losses approached a fairly constant value with a periodic ripple about this value as shown in Figure 2.8. Therefore, this periodic ripple was accounted for by repeating the loss calculations but plotting them against the equivalent Fresnel number instead of the Fresnel number. Figure 2.9 demonstrates how the diffraction losses can be minimized when $N_{eq}$ is a half-integer value and maximum when it is an integer value. Therefore, the unstable resonator design, presented later in Chapter 4, uses a half-integer value of $N_{eq}$

# CHAPTER III

## Measurements

### 3.1 Measurements of $I_s$ and $\gamma_o$ using the Rigrod equation

Two studies were done to measure the small signal gain coefficient, $\gamma_o$, and the saturation intensity, $I_s$, which are critical in determining the performance of a laser (power extraction, coupling, etc.). In the first study, $\gamma_o$ and $I_s$ of the $CO_2$ gas laser system at the LHMEL facility were measured simply by running the laser at a given output power and keeping all variables constant except one. In Eq. (2.8), the output power is dependent on various parameters, such as the output coupling, $t_2$, and the length, $l_g$, of the gain medium. The length of the gain medium is 210 cm, while the length of the cavity, L, is 355 cm.

In this study, three different output couplers were used to vary $r_2$ or $t_2$ ($t_2 = 1-r_2$), which produced three different measured output power values, $P_1$, $P_2$ and $P_3$. Thus, three different output intensities, $I_{out1}$, $I_{out2}$ and $I_{out3}$ were calculated from these output powers using $I = P/Area$. By using two of the three output intensities, the corresponding reflectances ($r_2$) and output couplings ($t_2$), the Rigrod equation, Eq. (2.8), was used to solve for $\gamma_o$ and $I_s$. The setup for the first study is shown in Figure 3.1.

The beam splitter (B.S.) in Figure 3.1 is a ZnSe 2%/AR optic. It splits the 10.6 μm beam between the University of Dayton's ballistic calibrator (UDBC) and the integrating sphere. The integrating sphere is a hollow sphere which has the interior coated with a substance (infragold, NIR-FIR) that is nearly a perfect diffuse reflector. Light that enters the sphere is reflected from the wall and distributed uniformly around the interior. A thermopile detector is placed at a hole in the sphere wall, which samples the reflected light. A baffle is located inside to prevent the detector from having a direct view of the input beam.[10] The thermopile is a thermoelectric, voltage-generating device and, therefore, requires no bias voltage or current for operation. The UDBC is used to calibrate the integrating sphere. It consists of a number of thermocouples that converts the heat of the laser beam into a voltage that is plotted on graph paper using a x-y plotter. Each grid square on the graph paper is equal to 1 cm. A curve is produced on the x-y plotter from the UDBC and the number of grid squares is counted under the curve. A calibration of the UDBC given by the National Institute of Standards and Technology (NIST), which is[11]

709.36 Joules/(cm grid square).

Every year the NIST calibrates the UDBC. The calibration date for these measurements was May, 1996. The amount of energy in joules is calculated from

$$P = \left( \frac{709.36 Joules}{cm \cdot square} \right) \cdot \left( \text{number of cm grid squares} \right). \qquad (3.\ 2)$$

The computer records the resulting calibrated thermopile voltage, laser operation time, discharge voltage and current, cavity pressure, $CO_2$ fraction, $N_2$ fraction, and the He fraction. The laser has two sections, A and B, where the discharge current in each section is recorded. For all measurements the total current, $I_A + I_B$, started from 2.5 amps and was ramped down to 0.0 amps with the $CO_2$:$N_2$:He gas mixture of 1:5:30 and the cavity pressure between 49 and 52 Torr.

After the laser was aligned with the 75% coupler, a calibration run of the laser was taken. The x-y plotter produced 12.6 cm grid squares under the UDBC curve, which, when multiplied by 709.36 J/(cm grid square) gives a calibration factor of 8938 J of energy produced by the laser. The plot of the signal from the integrating sphere is shown in Figure 3.2.

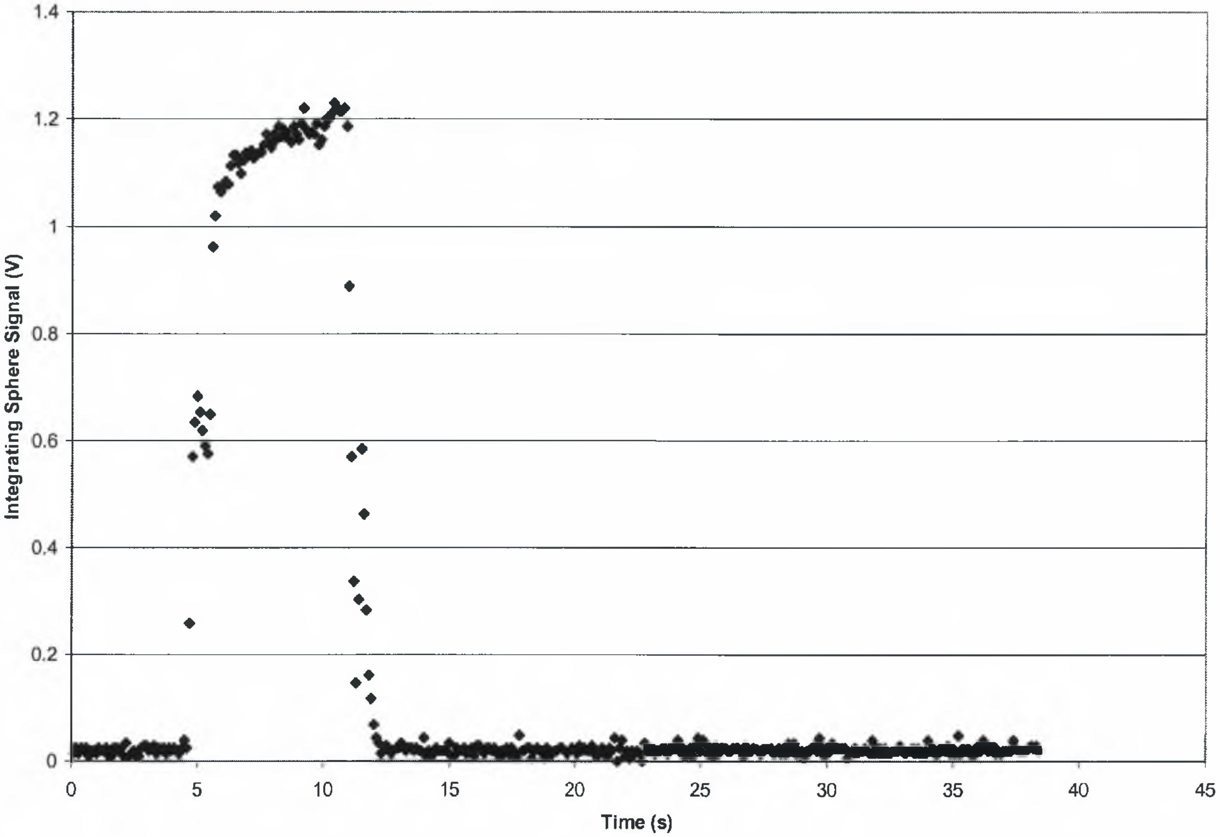

**Figure 3.2**. Integrating sphere signal with the 75% coupler for 8938 J laser output.

As shown in Figure 3.2, lasing occurred between 4.8 and 11 s for an interval of 6.2 s and an *average* integrating sphere voltage of 1.1 V. The laser energy of 8938 J divided by the time interval gives an average power for the 75% coupler of 1442 W. The calibration factor for the 75% coupler, $C_{75}$, can be found by

$$C = \frac{\text{Laser Power (W)}}{\text{Integrating Sphere Signal (V)}}, \qquad (3.\ 3)$$

$$C_{75} = \frac{1442\ \text{W}}{1.081\ \text{V}},$$

$$C_{75} = 1333\frac{\text{W}}{\text{V}}.$$

By the same process the calibration factors were found for the 17%/AR and 60%/AR couplers. The results are given in Table 3.1.

**Table 3.1**. Calibration factors for the three output couplers.

| | |
|---|---|
| $\mathbf{C_{17}}$ | 1153 W/V |
| $\mathbf{C_{60}}$ | 1159 W/V |
| $\mathbf{C_{75}}$ | 1333 W/V |

The 17% and 60% calibration factors differ from the 75% calibration factor because the 75% coupler data was taken at a later date after the system has been completely realigned.

A plot of output power verses loaded input power can then be made as shown in Figure 3.3 for the 75% coupler, where

$$\text{Input Power} = (\text{Power Supply Voltage})\left[(\text{Current } I_A + \text{Current } I_B)\right]. \tag{3. 4}$$

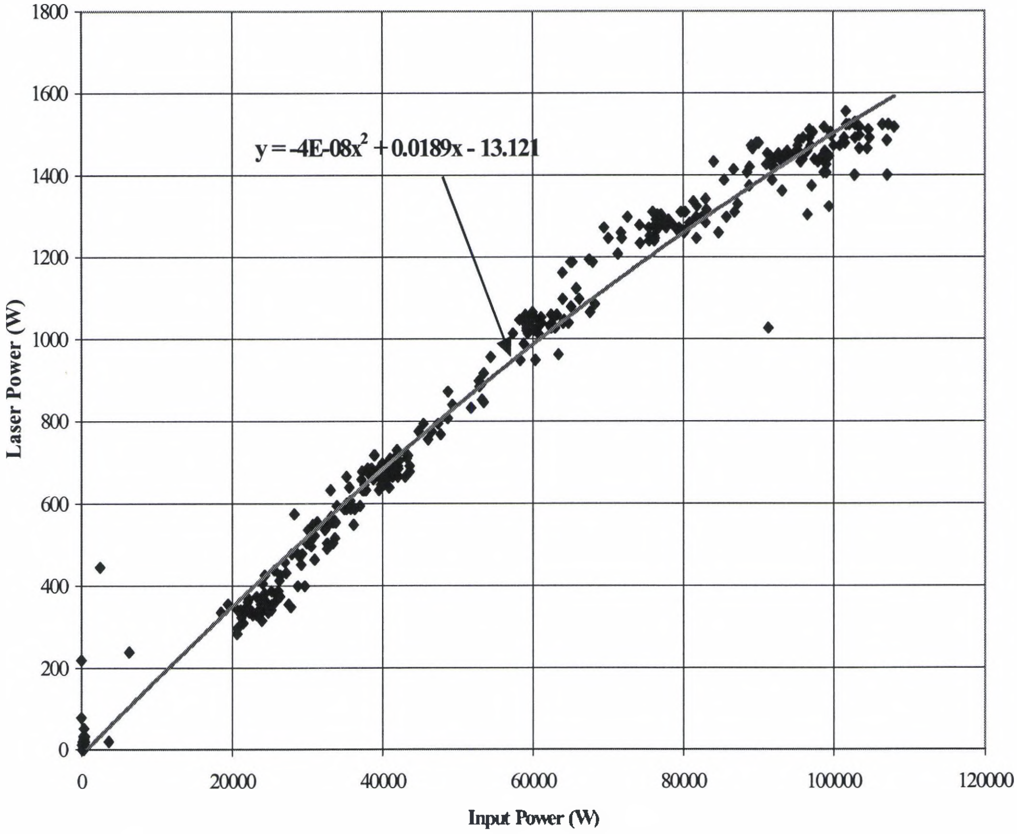

**Figure 3.3.** Laser Power characteristics using the 75% coupler.

The plot follows a second order polynomial. The equation, which fit the data in Figure 3.3, is given by

$$P_{out} = k_0 + k_1 P_{in} + k_2 P_{in}^{\ 2}. \tag{3. 5}$$

In this equation, $P_{in}$ is equal to the loaded input power and $P_{out}$ is equal to the output power.

By a similar process, the data for the 17%/AR and 60%/AR couplers were collected and analyzed. Table 3.2 displays the coefficients of Eq. (3.5) for each coupler.

**Table 3.2**. Polynomial coefficients for each coupler.

| | $k_2$ | $k_1$ | $k_0$ |
|---|---|---|---|
| $P_{out}$**(17%)** | $-1x10^{-7}$ | 0.0329 | -757.38 |
| $P_{out}$**(60%)** | $-9\ e^{-8}$ | 0.0269 | -976.34 |
| $P_{out}$**(75%)** | $-4x10^{-8}$ | 0.0189 | -13.21 |

The polynomial fits were used to calculate the output power so that the output intensity could be determined by dividing the output power by the area of the beam, which is a uniform circular irradiance pattern. All three couplers had the same diameters of 3.0-cm (1.18 inches). Thus, the area of the beam out is 7.07 $cm^2$.

In order to compute $\gamma_o$ and $I_s$, the value of the input power into the system was chosen to be 70 kW for each coupler. This value was chosen because it corresponds to 1.75 A. In the second study described in the next section, 1.75 A was also the operating current along with 49-52 Torr and the same gas mixture. Substituting 70 kW into the three polynomial equations for the three couplers gives the values in Table 3.3 and the corresponding intensities.

**Table 3.3**. Output powers and intensities for each coupler at 70-kW input.

| **Coupler** | **$P_{out}$(W)** | **$I_{out}$(W/cm$^2$)** |
|---|---|---|
| 17% | 465.7 | 65.9 |
| 60% | 1,056 | 149.3 |
| 75% | 1,114 | 157.6 |

The intensities in Table 3.3 were used with Eq. (2.8) to solve for $\gamma_o$ and $I_s$. This was done by using the pair of values $I_{out75}$ and $I_{out17}$ in Eq. (2.8), thereby providing two equations and two unknowns. The same was done with $I_{out60}$ and $I_{out17}$, but ***not*** for $I_{out75}$ and $I_{out60}$ because this pair of values was too close to give meaningful results. Now, from the Rigrod equation, Eq. (2.8), the mathematical computer program, MathCad, was used to solve for the two unknowns, $\gamma_o$ and $I_s$. The results are given in Table 3.4 for each coupler.

**Table 3.4**. Values for $\gamma_o$ and Is, obtained from coupler data.

| **Coupler Pair** | $\gamma_o$ **(cm$^{-1}$)** | **$I_s$ (W/cm$^2$)** |
|---|---|---|
| **75% & 17%** | 0.0067 | 131 |
| **60% & 17%** | 0.0066 | 137 |

## 3.2 Single-pass Measurements of $\gamma_o$

In this study, the small signal gain coefficient, $\gamma_o$, was directly determined by introducing a low-power Advanced Kinetics (A.K.) laser beam (30 W maximum output power) into the laser gain medium and measuring the amplified output after only *one* pass through the medium. This amplified signal is known as the single-pass, small signal power gain, $G_o$, is given by[4]

$$G_o = \frac{\text{Power Out}}{\text{Power In}} = \frac{P_{out}}{P_{in}}, \tag{3.6}$$

and is related to $\gamma_o$ by

$$G_o = \exp(\gamma_o l_g). \tag{3.7}$$

Using the measured value of $G_o$, from Eq. (3.7), $\gamma_o$ can be solved

$$\gamma_o = \frac{1}{l_g}(\ln G_o), \tag{3.8}$$

where $l_g = 210$ cm.

The setup to measure $G_o$ is shown in Figure 3.4.

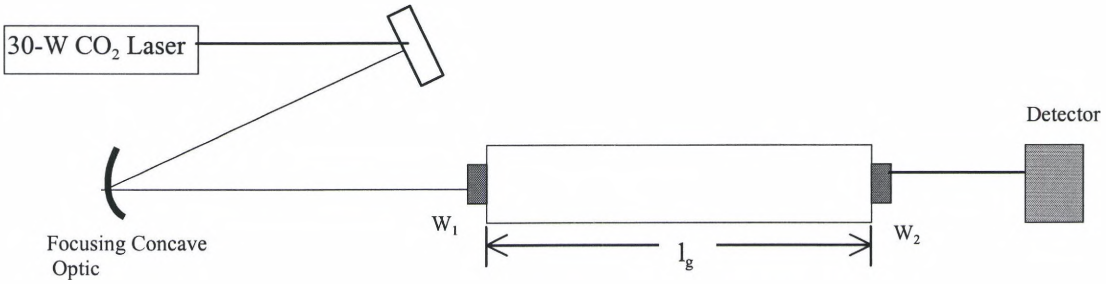

**Figure 3.4.** Setup for the single-pass $G_o$ measurement. $W_1$ and $W_2$ are the windows in contact with the laser medium.

In Figure 3.4, the A.K. laser system was adjustable, which allowed the laser system to be set to minimal output power. The beam diverges as it passes through the 355-cm laser cavity; therefore, a concave mirror with a ROC of 35 meters was used to reduce the divergence of the laser beam. With this arrangement, a burn pattern was taken of the laser beam at the input to the cavity and at the detector giving an input beam diameter of 1.0 cm and a beam diameter at the detector 1.5 cm. Since the detector diameter is about 5 cm, the detector power head collected the entire laser beam. The A.K. laser power supply was adjusted to produce a minimum output at the detector of 0.4 V (Note: the detector was coupled to the computer, which recorded the voltage output.) This small output was important to ensure that LHMEL I-R gain medium was not being saturated while $G_0$ was measured.

The windows, $W_1$ and $W_2$, were 3.8-cm thick ZnSe flats with one side having 1.0% reflectance and the other side 0.2% reflectance. The 0.2% reflectance surfaces faced towards the incoming A.K. laser beam. The windows were witness samples and were also wedged, so $W_1$ was tilted counterclockwise and $W_2$ was tilted clockwise (about the z-axis) to prevent any lasing inside the cavity. Only one detector was needed because the A.K. laser was continuously running throughout the entire experiment, that is, before and during the excitation of the LHMEL I-R laser medium. The plot in Figure 3.5 illustrates a typical measurement run.

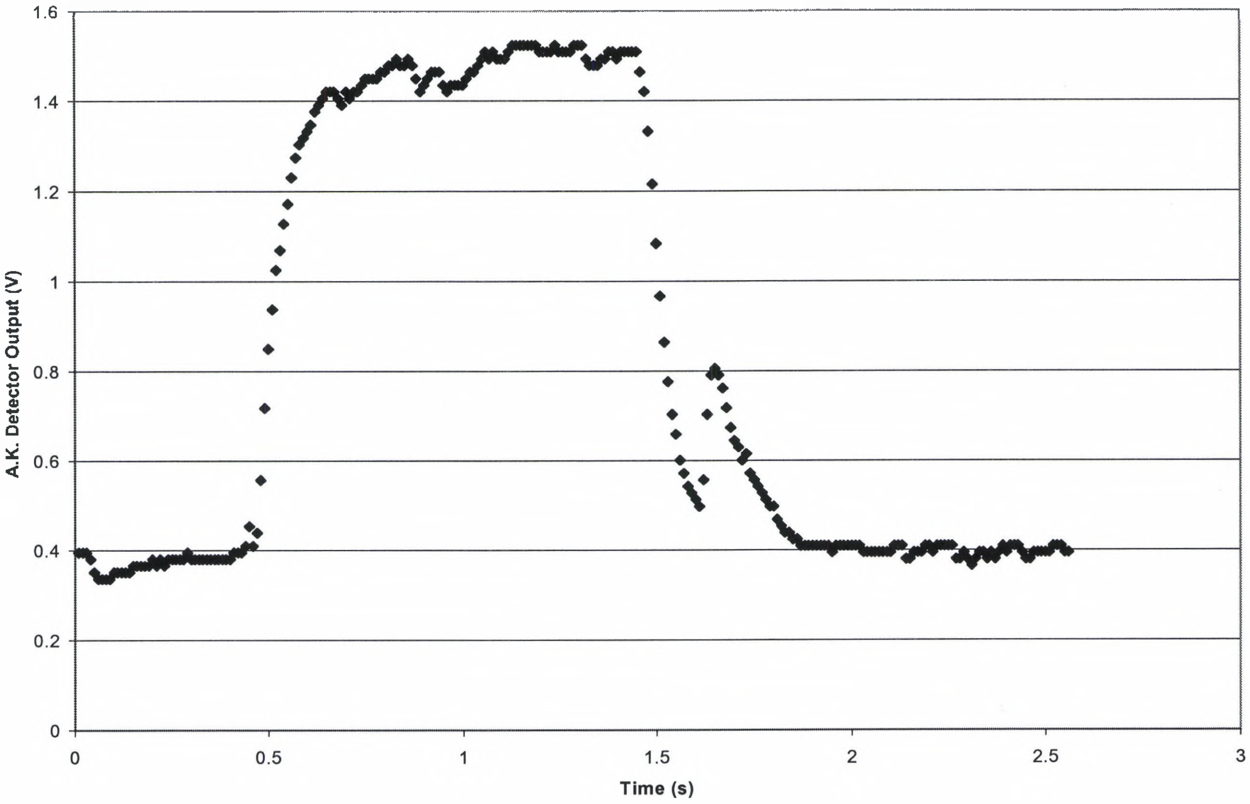

**Figure 3.5**. Detector output verses time for single-pass, $\gamma_o$ measurements.

The analysis of the data in Figure 3.5 gives an average signal over 0.0-0.5 s and 1.9-2.55 s of 0.385 V. Likewise, the average detector output during 0.5-1.5 s when the plasma laser medium had gain was 1.48 V, which corresponds to $P_{out}$. The data in Figure 3.5 from 1.5-1.9 s was not considered. These data represent a flash (electrical short) that occurs in the plasma when the system is turned off. The small signal power gain, calculated from Eq. (3.7), is

$$G_o = 3.85$$

The resulting small signal gain coefficient becomes

$$\gamma_o = \frac{\ln(3.85)}{210 \text{ cm}},$$

$$= 0.0064 \text{ cm}^{-1}.$$

This procedure was repeated three times. The results of $\gamma_o$ are summarized in Table 3.5.

**Table 3.5**. $\gamma_o$ from the single pass gain measurements.

| **Run** | $\gamma_o$ **(cm$^{-1}$)** |
|---|---|
| **1** | 0.0064 |
| **2** | 0.0063 |
| **3** | 0.0064 |
| **Mean** | **0.0064** |

The values using the Rigrod equation and the single-pass $\gamma_o$ measurements are summarized in Table 3.6.

**Table 3.6**. Small signal gain coefficients from both experiments.

| | $\gamma_o$ **(cm$^{-1}$)** |
|---|---|
| **75% & 17% Coupler** | 0.0067 |
| **60% & 17% Coupler** | 0.0066 |
| **Single Pass** | 0.0064 |
| **Mean $\gamma_o$** | *0.0066* |

The same plasma current was used for both the Rigrod equation and the single-pass measurements. This current was determined from plots of detector output verses current. This is illustrated in Figure 3.6 for the single-pass $\gamma_o$ coefficient measurement. The plots for the Rigrod equation measurements are shown in Appendix C.

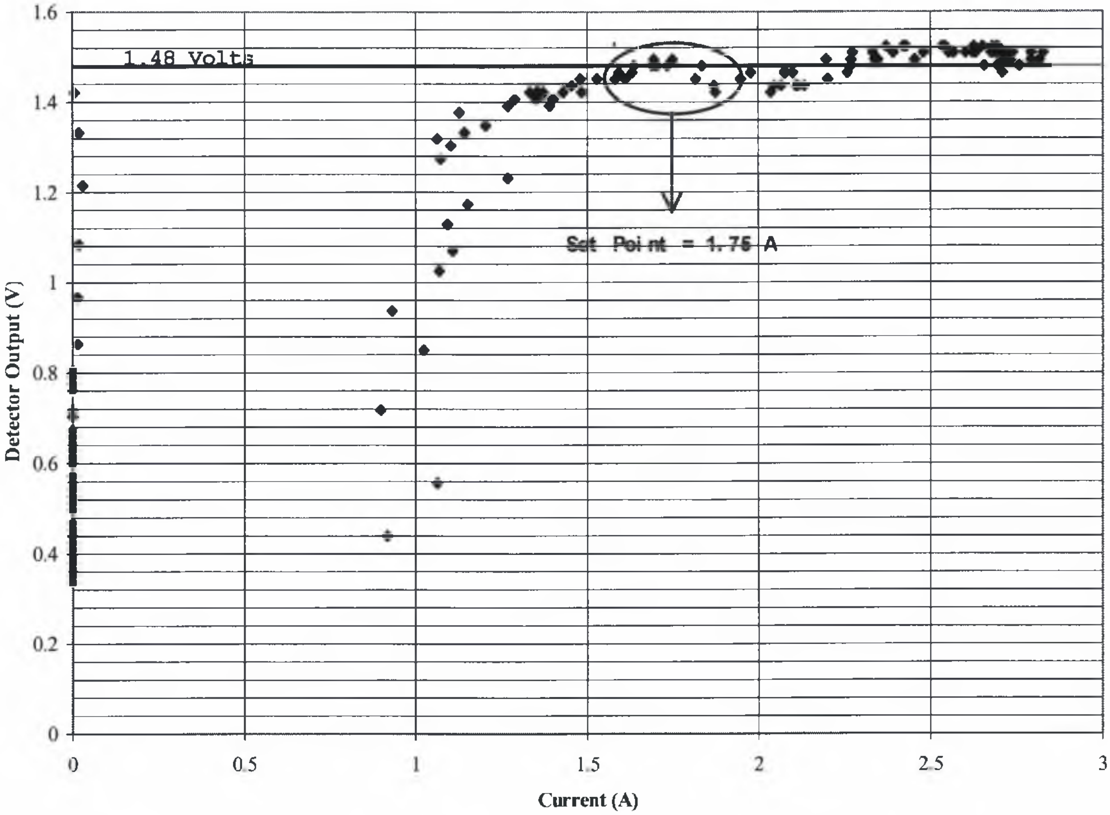

**Figure 3.6**. Detector output verses current for the signal-pass $\gamma_o$ measurement.

As shown in Figure 3.6, each study had the same current level of 1.75 A. The cavity pressures were in the range of 49 to 52 Torr. The gas mixtures were plotted against time and were essentially constant. Plots of the cavity pressures and gas mixtures are given in Appendix C.

Summarizing the results of the two studies, we found the small signal gain coefficient to range between 0.0064 and 0.0067 cm$^{-1}$, while the saturation intensity ranged from 130 to 136 W for the above specified conditions.

# CHAPTER 4

## Unstable Resonator Designs

### 4.1 Preliminary Unstable Resonator

Three unstable resonator designs initially considered were (a) positive-branch confocal, (b) negative-branch confocal, and (c) plano-convex illustrated in Figure 4.1.[7]

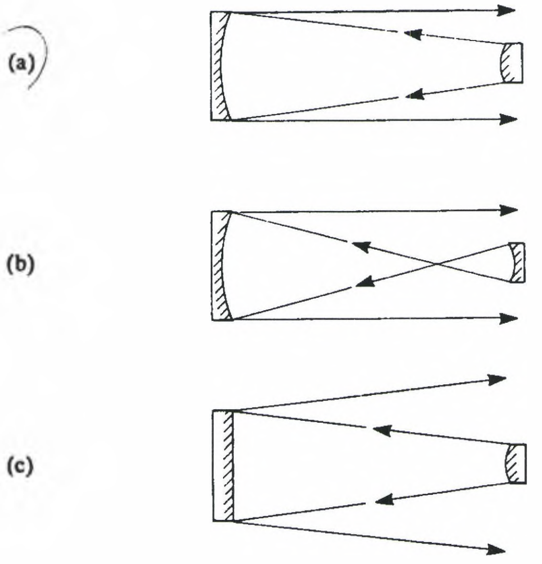

Three commonly used unstable resonator configurations
(a) Positive branch confocal ($g_1g_2 > 1$)
(b) Negative branch confocal ($g_2g_2 < 0$)
(c) Plano-convex

**Figure 4.1.** Unstable resonator configurations [from Reference No.7].

The positive-branch confocal unstable resonator shown in Figure 4.1(a) has the advantage of producing a collimated (plane wavefront) output beam. To generate a collimated output beam the back mirror, $M_1$, and the output coupler, $M_2$, must have a common focal point. The negative-branch confocal unstable resonator also generates a collimated output beam. It has an internal focus inside the cavity, as shown in Figure 2.1(b), which will cause a plasma breakdown in high power gas lasers due to the high internal irradiance at the focus. The plano-convex unstable resonator does not produce a collimated output beam and since the LHMEL facility currently owns a concave back mirror with a diameter equal to the diameter of the cavity, this choice was eliminated. Thus, the clear choice for the conventional unstable resonator is the positive-branch confocal resonator.

The specifications for the output coupler, $M_2$, were based on the characteristics of the available back mirror, $M_1$. It has a radius of curvature, $R_1$, of 3500 cm and a diameter, $2a_1$, of 10.16 cm. Since the mirrors, in the confocal design, have a common focal point they can be described by

$$\frac{R_1}{2}+\frac{R_2}{2}=L\quad, \tag{4. 1}$$

where L is the length of the cavity.

The length of the $CO_2$ laser cavity is 355 cm from $M_1$ to $M_2$, therefore $R_2$ = -2790 cm (convex). The magnification can then be solved by

$$M=\left|\frac{R_1}{R_2}\right|=\frac{35.00m}{27.90m}=1.254\,. \tag{4. 2}$$

The loss due to the output coupling, $L_c$, is given by[7]

$$L_c=1-\frac{1}{M^2}\,, \tag{4. 3}$$

or

$$L_c = 1 - \left(1 - \frac{2L}{R_1}\right)^2 . \tag{4.4}$$

Thus, $L_c = .364$ or 36.4% of the radiation is coupled out of the resonator. The radius of the output coupler, $a_2$, can be found from

$$a_2 = a_1\sqrt{(1 - L_c)}, \tag{4.5}$$
$$= 4.05 \text{ cm.}$$

It is useful to characterize this resonator design with the g-parameters and to determine the ray-tracing transmittance matrix.[4] For this design $g_1 = 1 - \frac{L}{R_1} = 0.898$, and $g_2 = 1 - \frac{L}{R_2} = 1.127$. The product of $g_1$ and $g_2$ is $g = g_1 g_2 = 1.013$, and since $g>1$ this confirms that the value determined for $R_2$ gives an unstable resonator.

The ray-tracing ABCD transmittance matrix was calculated for a ray that starts just before $M_1$ and after one round-trip it ends up at $M_1$. Figure 4.2 depicts this process.

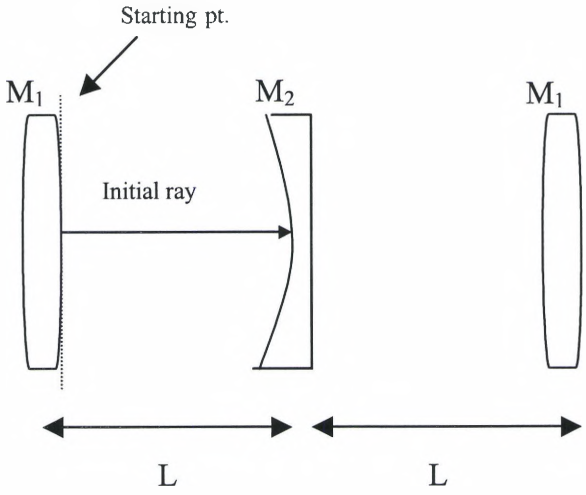

**Figure 4.2.** Equivalent-lens waveguide for the cavity in Figure 4.1 (a).

The transmittance matrix, T, for Figure 4.2 is given by

$$T = \begin{pmatrix} 1 & 0 \\ -\dfrac{2}{R_1} & 1 \end{pmatrix} \begin{pmatrix} 1 & L \\ 0 & 1 \end{pmatrix} \begin{pmatrix} 1 & 0 \\ -\dfrac{2}{R_2} & 1 \end{pmatrix} \begin{pmatrix} 1 & L \\ 0 & 1 \end{pmatrix}, \tag{4. 6}$$

$$T = \begin{bmatrix} \dfrac{(R_2 - 2L)}{R_2} & 2L\dfrac{(R_2 - L)}{R_2} \\ -2\dfrac{(R_2 - 2L + R_1)}{(R_1 R_2)} & \dfrac{(-4LR_2 + 4L - 2LR_1 + R_1 R_2)}{(R_1 R_2)} \end{bmatrix}, \tag{4. 7}$$

$$T = \begin{pmatrix} 1.254 & 800.3 \\ 0 & .797 \end{pmatrix} = \begin{pmatrix} A & B \\ C & D \end{pmatrix},$$

where the stability criteria can also be determined from the transmittance matrix elements A and D by

$$0 \leq \frac{(A + D + 2)}{4} \geq 1. \tag{4. 8}$$

Here the matrix elements A and D are given as

$$A = 1.254 = M, \tag{4. 9}$$

$$D = 0.797 = \frac{1}{M}. \tag{4. 10}$$

These values give

$$g = \frac{(A + D + 2)}{4} = 1.0127 \tag{4. 11}$$

which agrees with the g-parameters analysis previously mentioned.

By using the ABCD matrix, the number of passes that a ray will make in a resonator can be theoretically determined. The general solution for a ray positioned from the axis for s round-trips inside the resonator is[4]

$$r_s = r_a \cdot \left(F_{pos}\right)^s + r_b \cdot \left(F_{neg}\right)^s, \tag{4. 12}$$

where the constants $r_a$ and $r_b$ are

$$r_a = \frac{1}{\left(F_{neg} - F_{pos}\right)} \cdot \left[h \cdot \left(F_{neg} - A\right) - B \cdot m\right], \tag{4. 13}$$

$$r_b = \frac{1}{\left(F_{pos} - F_{neg}\right)} \cdot \left[h \cdot \left(F_{pos} - A\right) - B \cdot m\right]. \tag{4. 14}$$

When h = 0 the ray will never leave the cavity because at exactly on axis the mirrors are perpendicular to the ray. Therefore, in order for the ray to exit the cavity, an initial off-axis position of h = 1 mm at $M_1$ was chosen. We also let m = 0, which is the slope of the initial ray. A and B are matrix elements from the ABCD transmission matrix. $F_{pos}$ and $F_{neg}$ are given by[4]

$$F_{pos} = \frac{(A+D)}{2} + \left[\left(\frac{A+D}{2}\right)^2 - 1\right]^{.5} \tag{4. 15}$$

$$F_{neg} = \frac{(A+D)}{2} - \left[\left(\frac{A+D}{2}\right)^2 - 1\right]^{.5}. \tag{4. 16}$$

Here, D is obtained from the ABCD matrix.

The number of passes are calculated using Eq. (4.12) by computing Eqs. (4.13) – (4.16) for a particular resonator. Using the values in Eq. (4.7), we computed **s** from 1 to 17. These values are given in Table 4.1. Since the rays from $M_1$ are parallel to the axis, when the position of the ray from the axis exceeds the radius of the smallest mirror (the output coupler in this design), it exits the resonator. The output coupler has a radius, $a_2$, of 4.05 cm. We see in Table 4.1 that on the 17th round-trip the ray exits the resonator.

**Table 4.1.** Position, $r_s$, of a 1-mm off-axis ray at $M_1$ after s round-trips.

| s | $r_s$ cm | s | $r_s$ cm | s | $r_s$ cm | s | $r_s$ cm | s | $r_s$ cm |
|---|---|---|---|---|---|---|---|---|---|
| 1 | 0.13 | 5 | 0.31 | 9 | 0.77 | 13 | 1.91 | 17 | 4.72 |
| 2 | 0.16 | 6 | 0.39 | 10 | 0.97 | 14 | 2.39 | | |
| 3 | 0.20 | 7 | 0.49 | 11 | 1.21 | 15 | 3.00 | | |
| 4 | 0.25 | 8 | 0.61 | 12 | 1.52 | 16 | 3.76 | | |

Diffraction effects that distort the propagating wavefront will be present in this design, therefore the Fresnel and equivalent Fresnel numbers were calculated for this design. The Fresnel number, N, is equal to 43.6, and $N_{eq}$ is equal to 5.55. As discussed in Section 2.2, for minimal diffraction loss, a half-integer value is suggested (5.5). From the Fox and Li plots (Figures 2.8 and 2.9), approximately a 20% power loss per one-way bounce due to diffraction for a g-parameter of 1.013 will occur in this design.

For simplicity, this design uses Eq. (2.8), which actually applies to stable resonators, to theoretically calculate the approximate output irradiance. However, this design is in close proximity to a stable cavity since it consists of many round trips and the g-parameter is close to 1.0. The output power can be obtained by multiplying this irradiance by the beam area. The area of the output beam is found from taking the difference between the area of the cavity (or back mirror) and the area of the front mirror, which gives 29.511 cm$^2$. To calculate the output irradiance, the coupling, $T_2 = L_c$, (the output beam around the front mirror) has to be used as a "pseudo" value for the reflectivity, $r_2$. Thus, $L_c = T_2 = 1\text{-}r_2$ or $r_2 = 0.636$. Using $I_s = 135$ W/cm$^2$ and $\gamma_o = 0.00657\text{-cm}^{-1}$, the output power is found to be approximately 3.5 kW.

## 4.2 Unobscured Unstable Resonator

Another design was considered in order to avoid the annular output beam of the previous design due to the light exiting the resonator *around* the output coupler.[13] This design is known as the unobscured unstable resonator. In this design the output beam exits through an aperture. Figure 4.3 indicates how the front (annular) mirror, $M_2$, has a hole in the center which acts as the aperture. The aperture represents the output coupling of the resonator.

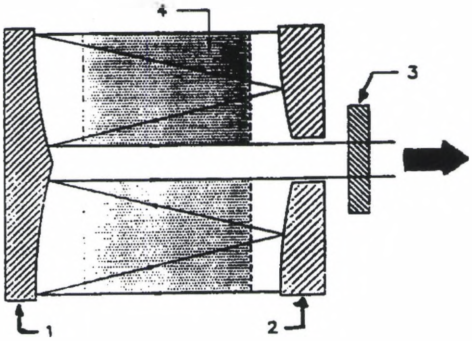

**Figure 4.3.** Unobscured unstable resonator design. (1) concave (toric) mirror, $M_1$, (2) convex (annular) front mirror, $M_2$, (3) ZnSe output window, (4) discharge volume.

The simplicity of this unobscured design is that the ROC of both mirrors, $M_1$ and $M_2$, are initially determined in the same manner as for the unstable confocal resonator design given in the previous section. The next step in the design process is to "cut and flip" the unstable confocal resonator mirrors to form a toric back mirror and an annular front mirror. A diamond turning process, which starts at the center of the copper optic usually produces the back toric mirror, $M_1$. The center-of-curvature of the toric and annular mirrors are at the edges, whereas in the unstable confocal design, the center-of-curvatures are on the optical axis of the resonator. The size of the hole is the output coupling of the resonator that is sealed by a ZnSe window. The objective of the design process is to determine the optimum size of this hole or output aperture.

The optimal coupling for any resonator can be determined by plotting output power ($P_{out}$) verses output coupling ($L_c$). Again, the output power can be calculated using Eq. (2.8) and the area of the output beam. It uses the same mathematical equations as an unstable confocal resonator, but the optics are essentially "cut and flipped" to form the *unobscured* unstable confocal design. For the unobscured unstable design presented here, the area of the output beam changes as the coupling or aperture changes, this is graphically shown in Figure 4.4.

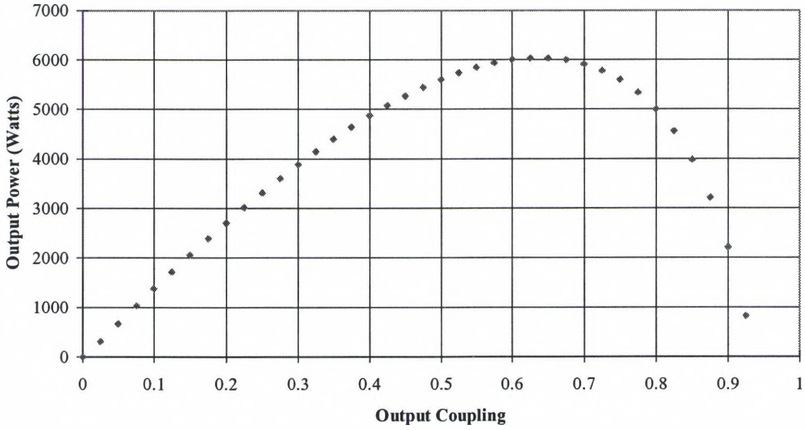

**Figure 4.4.** Output power verses coupling for the unobscured unstable resonator with $I_s = 135\ W/cm^2$ and $\gamma_o = 0.00657\ cm^{-1}$.

Figure 4.4 shows, for this design, the optimal output power is between 60% and 70% coupling. At best, only 6.0 kW will be extracted from the unobscured unstable design (only 2.5 kW more than the preliminary design), which is considerably less than the current stable resonator at the LHMEL facility. The stable resonator has an experimental maximum output power of approximately 14.0 ± .25 kW, which was also confirmed theoretically using Eq. (2.8). The LHMEL facility's stable resonator utilizes most of the gain medium because the resonator is similar to a plane-parallel resonator described in Section 2.2. A plane-parallel resonator will use the entire gain medium available since both mirrors are flat. The back mirror, of the stable resonator, is fairly flat (ROC = 355 cm) and the front coupler is flat, therefore most of the gain medium is utilized. Second, the stable resonator has more round-trips through the gain medium. Third, the output beam of the stable resonator has a larger theoretical diameter[14] (9.889 cm – see Appendix B) since the light is coupled through a partially reflective flat mirror and not through an aperture, or output coupler, as in the unobscured unstable resonator. The aperture of the unobscured unstable resonator forms the output beam profile, which now needs to be considered. What coupling will yield the best beam profile? A team of Canadian scientists, Yelden, Seguin, Capjack and Nikumb, at the University of Alberta[15] did a study that also applied an unobscured unstable resonator[13] and found that the quality of the output beam is dependent on the size of the aperture. Thus, a smaller aperture will be more likely to produce a Gaussian-type beam profile in the near field, whereas, a larger aperture will be more likely to produce an annular output beam profile. Fundamentally, when the area of the aperture becomes smaller, the Rayleigh range, $z_r$, reduces and makes the Fraunhofer region closer. Thus, the near-field or Fresnel region becomes shorter, and a Gaussian beam is viewed after less beam propagation. Since the waist of the output beam is at the aperture, the Rayleigh range is effectively the area of the aperture divided by the wavelength ($z_r = \pi a^2/\lambda$, for a circular aperture). For a single-lobe-type beam profile (similar to a Gaussian beam, in that it has essentially one smooth central lobe) an expression of the form $z = \pi a^2/\lambda$ can be used to estimate the propagation characteristics of the beam. Namely, the far-field limit is when $z >> z_r$, and for the near-field the limit, $z < z_r$.

A computer program[11] was used to simulate this concept, with LHMEL I laser dimensions, but for various aperture diameters (for different couplings). The results are given in Figure 4.5 and in Table 4.2.

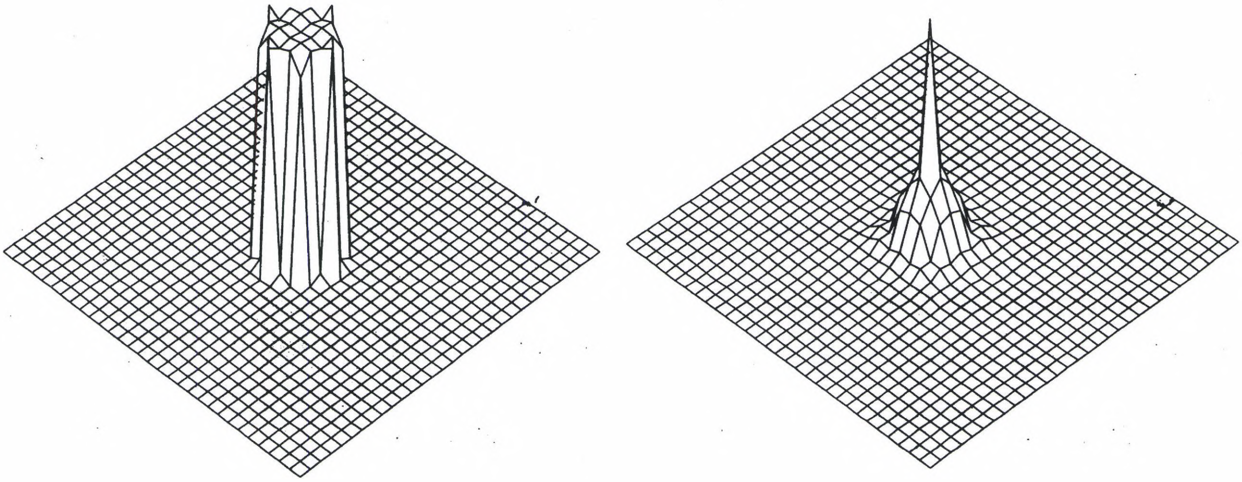
(a) (b)

**Figure 4.5**. Computer simulation of a non-Gaussian, single-lobe beam. (a) Near-field pattern (b) Far-field pattern.

Figure 4.5 demonstrates how near- and far-field patterns will look for the unobscured unstable resonator. Different size apertures were simulated to demonstrate how far the output beam would need to propagate to form a beam profile that has characteristics similar to a Gaussian beam. Table 4.2 shows the unobscured beam propagation distances for the computer simulations that gives a “Gaussian-type” of profile as in Figure 4.5 (b), and Table 4.2 also shows the Rayleigh range for a Gaussian profile formation.

**Table 4.2.** Various aperture areas and couplings that yield different distances for the computer simulation Gaussian-type of profile versus the Rayleigh range Gaussian profile. The couplings were first chosen then the aperture diameters and Rayleigh ranges were calculated. The computer calculated the computer simulation distances once the Gaussian-type profile in Figure 4.5 (b) was obtained by the computer.

| **Aperture Diameter** | **Coupling** | **Computer Simulation m** | **$z = \pi a^2/\lambda$ m** |
|---|---|---|---|
| 8.798 cm | 75% | 145 | 574 |
| 8.5 cm | 70% | 136 | 535 |
| 8.192 cm | 65% | 129 | 497 |
| 7.87 cm | 40% | 117 | 459 |
| 4.544 cm | 20% | 39 | 153 |
| 3.212 cm | 10% | 20 | 76 |

Table 4.2 shows how far the output beam must propagate from the unobscured unstable resonator (for various couplings) in order to form a Gaussian-type beam profile, similar to that in Figure 4.6 (b). After the output beam propagates the required distance to give a Gaussian-type beam profile, the Fresnel number, N, will be unity or slightly higher. Thus, there will be a smoother transverse mode pattern observed in the far field region.

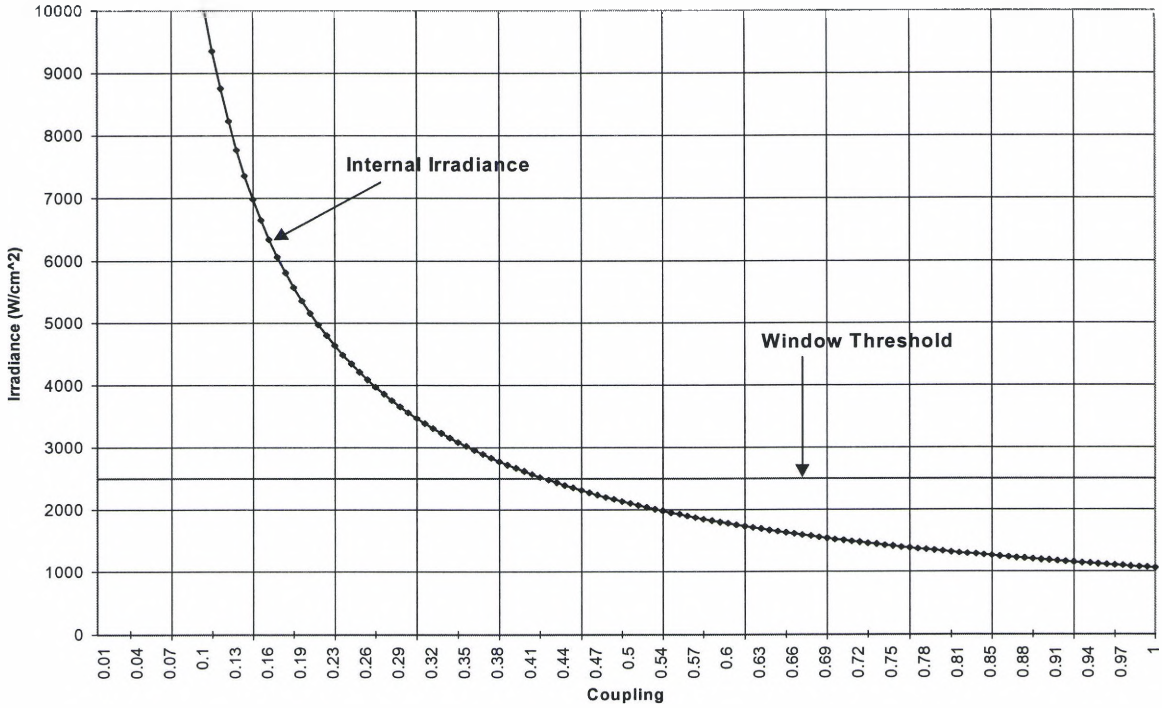

**Figure 4.6**. Internal irradiance inside the laser cavity verses coupling. The coupling cannot go below $L_c = 0.42$, otherwise the ZnSe window will be damaged.

In Figure 4.3, a ZnSe output window is shown. This window holds the laser system's vacuum which maintains the gain medium. There is a threshold irradiance of 2.5 kW/cm$^2$ that this window can endure before it is destroyed. Therefore, in Figure 4.6, a plot of internal irradiance verses output coupling was made to determine the coupling, which produces an internal irradiance of 2.5 kW/cm$^2$ or less.

Figure 4.6 demonstrates that the coupling must be greater than 42% in order to protect the very expensive ZnSe window needed for the unobscured unstable resonator. From

Table 4.2, a distance of 117 m or greater will be required for a quasi-Gaussian output beam. This is not a realistic distance for propagation, simply because it requires too much space. Therefore, a higher coupling will be chosen for more output power, to preserve the ZnSe window and for the possibility of allowing for lowest-order mode operation (which is discussed below).

The final result of the Rigrod analysis given in terms of losses as derived in Appendix A, is given in Eq. (4.17). This equation can be plotted with the ratio of the second to first mode mean irradiance levels ($I_2/I_1$) verses the output coupling. The second and first mode mean irradiance levels are spatially averaged irradiances, which are derived from the integral over the irradiance pattern for both of the first and second modes.[13] This plot evaluates the optimal output coupling to favor the lowest-order of transverse mode pattern to be self-reproducing in the laser resonator.[13]

$$\frac{I_{out}}{I_s} = \frac{L_c}{2}\left[\frac{2\gamma_o l_g + \ln\{(1-L_m)(1-L_m-L_c)\}}{\left[(L_m+L_c)+L_m\sqrt{\frac{(1-L_m-L_c)}{(1-L_m)}}\right]}\right] \tag{4.17}$$

According to Dr. James Reilly of Norgheast Science and Technology,[13] the spatially averaged irradiance $I_2$ is expressed as the round-trip small-signal cavity gain, $2\gamma_o l_g$, plus twice the losses due to output coupling, $2\ \ln(1\text{-}L_c)$.[13] The spatially averaged irradiance of the first order transverse mode $I_1$ is defined as the round-trip small-signal cavity gain, $2\gamma_o l_g$, plus the losses due to output coupling, $\ln(1\text{-}L_c)$.[13] Here $\gamma_o$, again, is the small signal gain coefficient, $l_g$ is the single-pass length of the gain medium, $L_m$ is the total loss (absorption and scattering) of each optic and $L_c$ is the output coupling. The ratio of the transverse mode irradiance levels measures the percent of first order to second order modes that will be self-reproducing in the laser resonator. For example, if the ratio of the spatially averaged irradiances, $I_2/I_1$, is equivalent to 0.1, then the second-order transverse mode is running in the cavity with 90% of the total power in the first order transverse mode, assuming $I_T = I_1 + I_2$. Hence, 91% of the output flux will be in the first-order mode, while 9% of the output flux will be in second-order mode. Any other transverse modes that may exist in the cavity will either be a small portion of the 9% or be surpressed out by the high output coupling losses.

Figure 4.7 illustrates how for $2\gamma_o l_g = 2.52$ ($\gamma_o = 0.006\ \text{cm}^{-1}$, $l_g = 210$ cm) the optimal output coupling becomes approximately 70%. For $2\gamma_o l_g = 2.73$ ($\gamma_o = 0.0065\ \text{cm}^{-1}$) the optimal output coupling is approximately 75%. An output coupling of 70% was chosen because of the concern that such a "thin" copper annular mirror would realistically permit lasing to occur. There was more confidence in the resonator being able to lase with a 70% output coupling than with 75% coupling.

Using the chosen coupling, the curvatures can be determined. The diameter of the aperture can then be found starting with Eq. (4.3), which can be written as

$$M = \frac{-1}{L_c - 1}\left(\sqrt{(1 - L_c)}\right) \tag{4.18}$$

$$M = 1.826 .$$

The diameter of the back mirror, $M_1$, is determined by the diameter of the cavity, which is 10.16 cm in diameter. The coupling is set by the ratio of the area of the output aperture, $A_3$, to the area of $M_1$, $A_1 = 81.07\ \text{cm}^2$, given by

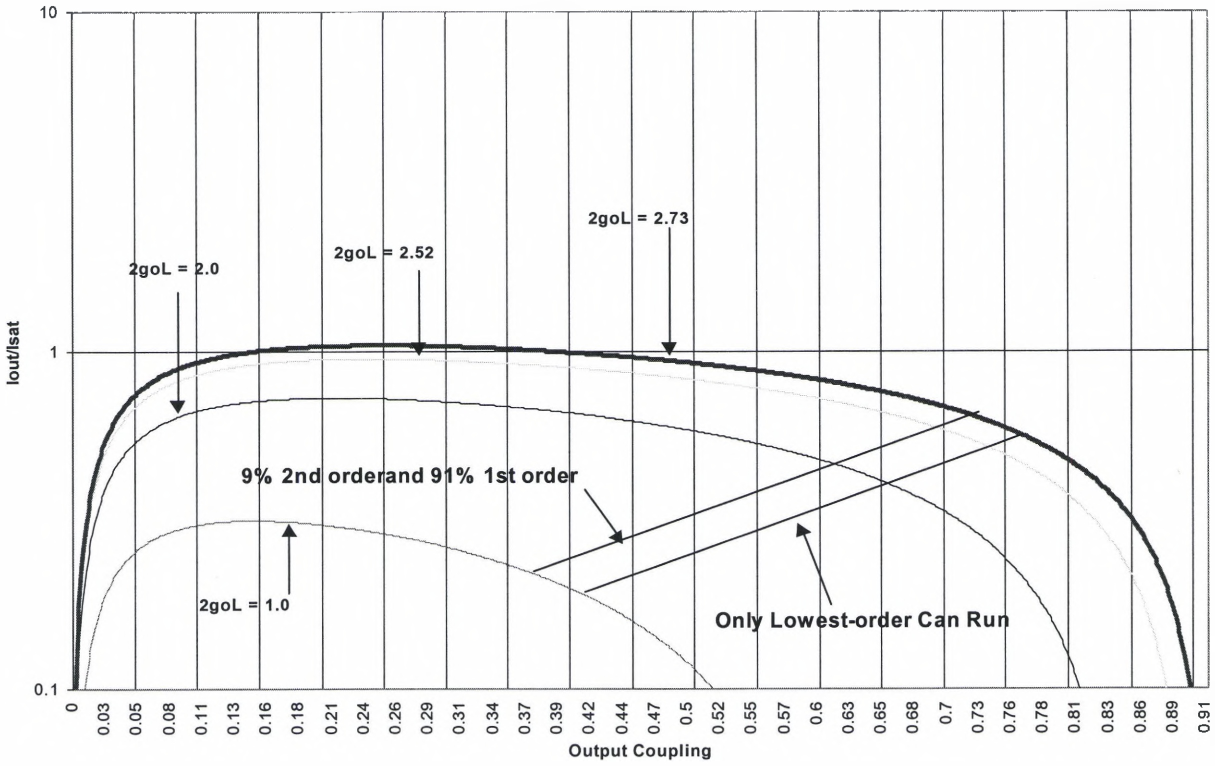

**Figure 4.7.** Normalized output irradiance and the ratio of the spatially averaged irradiance distribution verses the output coupling for the unobscured unstable resonator design. $I_2/I_1 = 10\%$, which favors a situation where the second- order mode is only 9% of the total output flux.

$$L_c = \frac{A_3}{A_1}. \tag{4.19}$$

Thus, with $A_1$ and $L_c$ we obtain $A_3 = 56.75\ \text{cm}^2$ with a radius of $a_3 = 4.25$ cm. The area of the annular front mirror, $A_2$, is given by

$$A_2 = A_1 - A_3. \tag{4.20}$$

$$A_2 = 24.3\ \text{cm}^2.$$

Thus, the radius of the front annular mirror, $a_2 = 2.78$ cm.

The radii of curvature, $R_{toric}$ and $R_{annular}$, must now be determined. The coupling is also equivalent to Eq. (4.4), with $R_{toric}$ replacing $R_1$ to give

$$L_c = 1 - \left[1 - 2\left(\frac{L}{R_{toric}}\right)\right]^2 , \tag{4.21}$$

where L equals the length of the cavity, 3.55 m. Solving for $R_{toric}$ we find

$$R_{toric} = \frac{1}{2L_c}\left[4L_c + 4\sqrt{L^2\left(L_c - 1\right)}\right] \tag{4.22}$$

Thus, $R_{toric}$ = 1.57 m. The radius of curvature for the front annular mirror, $R_{annular}$, is found by

$$R_{annular} = 2L - R_{toric} , \tag{4.23}$$

$$R_{annular} = -860 \text{ cm} .$$

A ray trace for the unobscured resonator design shows a ray makes thirteen passes before exiting the cavity through the aperture. This ray trace was completed using the same method as mentioned previously in Equations (4.6) to (4.16). The transmission matrix is given as

$$\mathrm{T} = \begin{pmatrix} 1 & 0 \\ \dfrac{-2}{\mathrm{R}_{\mathrm{toric}}} & 1 \end{pmatrix} \begin{pmatrix} 1 & L \\ 0 & 1 \end{pmatrix} \begin{pmatrix} 1 & 0 \\ \dfrac{-2}{R_{annular}} & 1 \end{pmatrix} \begin{pmatrix} 1 & L \\ 0 & 1 \end{pmatrix} ,$$

$$T = \begin{pmatrix} 1.826 & 1003 \\ 0 & .548 \end{pmatrix} .$$

The magnification, M, is equal to 1.826, and 1/M is equal to .548, which are given by the matrix elements A and D, respectively. This ray trace starts at the back toric mirror, M1, at a height, h, of 1 mm. The number of passes was also calculated as if the unobscured unstable resonator was a confocal unstable resonator. Essentially, the unobscured resonator is a conventional resonator because it possess the same optics, but they are "cut and flipped" to create the aperture instead of front mirror obstruction. The position of the ray, $r_s$, after the first round trip is 0.183 cm on the front mirror. This continues until the ray exits the resonator (through the aperture) for six round trips, and is shown in Table 4.3.

Table 4.3 shows five complete round-trips are made, but one more pass is made for the ray leaving the back toric mirror, $M_1$, and exits the cavity, thus 13 passes are made.

**Table 4.3**. Position, $r_s$, of a 1-mm off-axis ray at $M_1$ after s round-trips.

| **s** | $\mathbf{r_s}$ cm |
|---|---|
| 1 | .18 |
| 2 | .33 |
| 3 | 1.11 |
| 4 | 2.03 |
| 5 | 3.70 |
| 6 | 6.76 |

The Fresnel and equivalent Fresnel numbers were calculated for this design. The Fresnel number, N, is equal to 20.574, and $N_{eq}$ is equal to 8.494. As discussed in

Section 2.2, for minimal diffraction loss, a half integer value of $N_{eq}$ is needed. The near-field pattern will be similar to that in Figure 4.5(a), and the far-field pattern will be of the form of 4.5(b) after the output beam propagates approximately 136 m. If the output beam is of the lowest-order of transverse mode (from Figure 4.7), and if it is perfectly collimated then the beam can be focused down to an Airy Disk, which has a minimum diameter, S, of

$$S = \frac{2.44\,\lambda}{\mathrm{D}} f \quad , \tag{4.24}$$

Here, D is the diameter of the aperture (or beam which is 8.5 cm), $\lambda$ is the wavelength and f is the focal length of the lens. This is, at best, the smallest size to which the beam can be focused. Therefore, if a 150-cm focal length lens is used then a minimum diffraction limited spot will be 0.046-cm or approximately a 0.5 mm in diameter. At an output power of 6 kW, the irradiance will be approximately 3.6 $\mathrm{MW/cm^2}$.

# CHAPTER 5

## Unstable Resonator Using A Gaussian Variable-Reflectivity Coupler

Unstable resonators efficiently extract energy from large volume gain media; however, they have poor high-order mode discrimination and some designs generate beams with diffraction rings. These drawbacks, for any laser, are both due to finite apertures in or at the ends of any laser cavity. These aperture-edge diffraction effects can be smeared out using an output coupler with a radially varying reflectivity from its central maximum value down to zero at the edge. Since, the functional dependence of the reflectivity is typically Gaussian, the coupler is referred to as a Gaussian coupler.

This concept of Gaussian variable-reflectivity output couplers was investigated in a concave-convex unstable resonator[4] (similar to the conventional unstable resonator), shown in Figure 5.1.

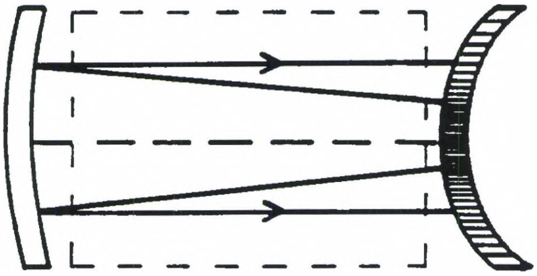

**Figure 5.1**. Concave-convex unstable resonator with a Gaussian variable-reflectivity convex output coupler.

Figure 5.1 shows a total reflecting concave mirror (left) and a Gaussian convex coupler (right) separated by a distance L, the cavity length. Chapter 12.9 in Verdeyen (third edition) states that the $1/e^2$ radius, $w_a$, for irradiance transmission through the Gaussian coupler is given by[4]

$$w_a = \sqrt{\frac{L\lambda}{\pi\left[\left(\frac{\sqrt{MX}}{2}\right)-\frac{X}{2}\right]}}, \tag{5. 1}$$

where X is defined as[4]

$$X = \frac{1}{2\pi \mathrm{N}} \tag{5. 2}$$

Here N is the Fresnel number (equaling 68.5) and M is the magnification. Referring back to Figure 4.6, a minimum coupling of 42% was determined to ensure that the ZnSe window would not be damaged. If the Gaussian coupler, made from ZnSe, will be made with 45% coupling, and the ratio of the R.O.C.'s of the back mirror (27.48 m) to the Gaussian coupler (-20.38 m) gives a magnification equal to 1.35. Thus, $w_a$ = 2.11 cm. The spot size, w, incident of the concave mirror is given by[6]

$$w = \sqrt{w_a^{\,2}\left(M^2-1\right)}, \tag{5. 3}$$

$$w = 1.91 \text{ cm}.$$

Now, $w_a$ and w are then used to compute the output beam profile given as[6]

$$I_{out}(r) = \left(1 - R_o \exp\left[\frac{-2r^2}{w_a^{\,2}}\right]\right)\exp\left[\frac{-2r^2}{w^2}\right], \tag{5. 4}$$

where r is the radius variable. The first term, in Eq. 5.4 is the radially increasing output coupler transmission, the second term is the radially decreasing Gaussian beam profile inside the resonator, and $R_o$ is the central value of the reflectivity for the Gaussian coupler.

Plots of $I_{out}$ verses the radius of the output beam, r, for various values of $R_o$ are shown in Figure 5.2.

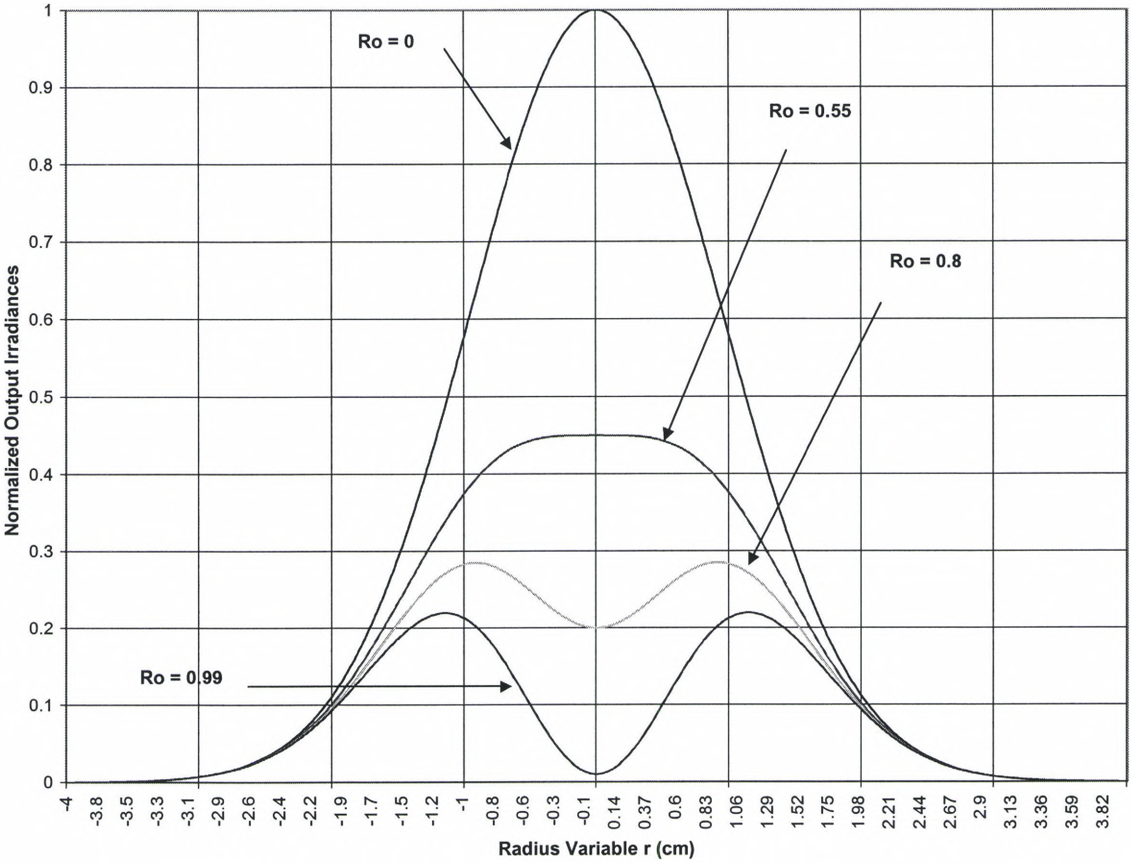

**Figure 5.2.** Normalized output irradiance, for different values of $R_o$, as a function of radius, r.

Figure 5.2 shows that the higher values of central reflectivity, $R_o$, produce more significant dips in the output beam profile. Therefore, it is important to choose $R_o$ such that it is not too small (where the laser oscillator will be over coupled), or too great (where the output beam will acquire a hole in the center). The central reflectivity is defined by[4]

$$R_o = \frac{1}{M^2}, \tag{5.5}$$

$$R_o = 0.55.$$

Figure 5.2 shows how $R_o = 0.55$ represents a "flat" condition where the central dip is about to appear. This will give the smoothest and most uniform output beam profile as shown in Figure 5.3.

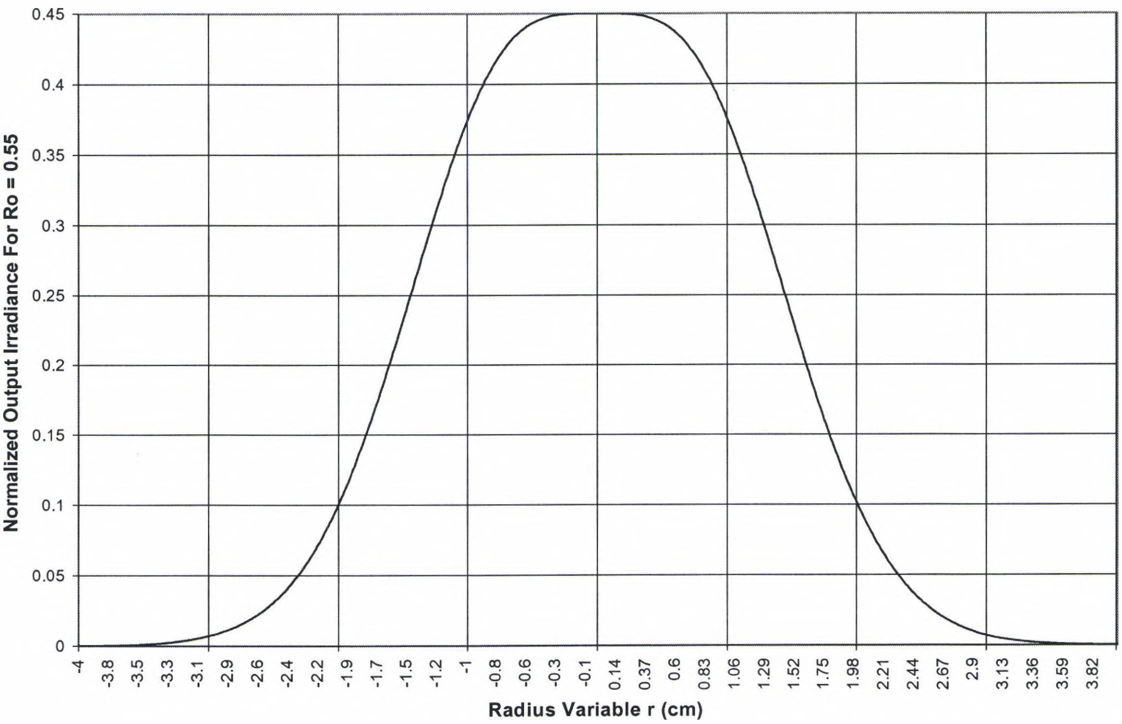

**Figure 5.3**. Output beam profile for $R_o = 0.55$.

Keeping Figure 5.3 in mind, the output coupler can be fabricated with a radially varying reflectivity from the center to the outer edge. The reflectivity function is given by[6]

$$R(r) = R_o \exp\left[-2\left(\frac{r}{w_a}\right)^2\right]. \qquad (5.6)$$

Table 5.1 lists the varying reflectivities on the Gaussian coupler. The central region, $R_o$, is 55% reflective, and then decreases until it reaches the edge of the Gaussian coupler where it is has nearly zero reflectivity. The Gaussian-coupler can be made either by tapered-reflectivity dielectric mirrors or by tapered-groove-depth diffraction gratings.[6] The tapered-reflectivity dielectric mirrors are not very easily fabricated for high power laser systems. A tapered-groove-depth diffraction grating is and more cost effective to manufacture for high power $CO_2$ laser systems. Etching a diffraction grating with a groove depth that varies from center to edge produces a tapered-grooved-depth diffraction grating. The smaller the interval between the groove depths the more difficult and *expensive* it is to manufacturer such a coupler. Therefore, Table 5.1 gives the reflectivity of the Gaussian coupler from the central position.

**Table 5.1**. Reflectivities of the Gaussian coupler.

| **Position** | **Reflectivity** |
|---|---|
| 0.0% -- center | 0.55 |
| 10% | 0.49 |
| 20% | 0.35 |
| 30% | 0.20 |
| 40% | 0.092 |
| 50% | 0.034 |
| 60% | 0.0098 |
| 70% | 0.0023 |
| 80% | 0.00043 |
| 90% | 0.000064 |
| 100% -- edge | 0.0000076 |

The average output coupling from this Gaussian output coupler is determined from the average reflectivity defined by[6]

$$r_{ave} = \frac{\int 2\pi r R_o \exp\left[-2\left(\frac{r}{w_a}\right)^2\right] \exp\left[-2\left(\frac{r}{w}\right)^2\right] dr}{\int 2\pi r \exp\left[-2\left(\frac{r}{w}\right)^2\right] dr} = \frac{R_o w_a{}^2}{\left(w^2 + w_a{}^2\right)} \exp\left[-2\left(\frac{r}{w_a}\right)^2\right] \quad , \qquad (5.7)$$

when r = 0 at the central position, then $r_{ave} = 0.55$. The average output coupling is then determined by

$$T_{ave} = 1 - r_{ave} \, ,$$

$$T_{ave} = 0.45 \, .$$

The Rigrod equation (Eq. 2.8) is modified to use these average quantities as

$$I_{out} = \left[ T_{ave} \frac{\gamma_o l_g - \frac{1}{2}\ln\left(\frac{1}{r_1 r_{ave}}\right)}{\left(1-\sqrt{r_1 r_{ave}}\right)\left(1+\sqrt{\frac{r_{ave}}{r_1}}\right)} \right] I_s$$

From Chapter 4, $I_s$ = 135 W/cm$^2$, $\gamma_o$ = .00066 cm$^{-1}$, $l_g$ = 210-cm and $r_1$ = .995 = reflectivity of the back mirror. The output power $P_{out}$ (*in the central lobe – referring to Figure 5.3*) will then be approximately 1.5 kW.

The Gaussian concave-convex design's ray trace is shown in Table 5.2.

**Table 5.2**. Position, $r_s$, of a 1-mm off-axis ray at the back mirror after s round-trips.

| s | $r_s$ cm | s | $r_s$ cm | s | $r_s$ cm | s | $r_s$ cm |
|---|---|---|---|---|---|---|---|
| 1 | 0.135 | 5 | 0.446 | 9 | 1.473 | 13 | 4.870 |
| 2 | 0.182 | 6 | 0.601 | 10 | 1.987 | 14 | 6.567 |
| 3 | 0.245 | 7 | 0.810 | 11 | 2.679 | 15 | |
| 4 | 0.331 | 8 | 1.093 | 12 | 3.612 | 16 | |

This design has twice as many round-trip passes as the unobscured design and approximately the same as the preliminary design, but produces considerably less output power than either of the first two designs. However, both the preliminary and the Gaussian coupler designs employ roughly the same amount of the gain medium considering the same number of round-trips are made. Also, the Gaussian coupler concave-convex design has a smaller output beam area (considering only the central lobe – in Figure 5.2) than either of the previous designs.

The focused spot size of a collimated Gaussian beam will be focused by a lens of focal length f, given by[6]

$$w_o = \frac{f\lambda}{\pi\, w_a(f)}\,, \tag{5. 8}$$

where $w_a(f)$ is the Gaussian spot size at the first surface of the lens (2.11 cm), f is the focal length and $w_o$ is the focused spot size. Therefore, if a 150-cm lens is used, the spot size, $w_o$, will be 0.024 cm or approximately 0.5 mm in diameter. This will produce an 830-kW/cm$^2$ irradiance distribution for an output power of 1,500 W.

After reviewing all three designs, the unobscured unstable resonator design was chosen. Table 5.3 below indicates the deciding factors.

**Table 5.3**. Advantages and disadvantages to each design.

| Options | Advantages | Disadvantages | Cost |
|---|---|---|---|
| Preliminary | Inexpensive. | Poor quality near-field beam. Spot size will not be very intense. | $ 6,000 |
| Unobscured | Reasonable cost, Small and intense spot size. Highest output power. | Fresnel-pattern for the near-field beam. | $ 11,000 |
| Gaussian | Small and intense spot size. Gaussian near-field beam. | Very expensive. Low output power. | $ 40, 000 |

Table 5.3 makes it apparent (from a cost standpoint) that the unobscured unstable resonator is the best choice[6]. The near-field beam will not be very useful, as illustrated

in Figure 4.5(a), but if operating in the lowest-order transverse mode it will produce an output focused beam diameter of 0.5 mm using a 150-cm lens. This produces approximately an output irradiance of 3.6 MW/cm$^2$ for 6 kW. In addition, this design can easily be converted into a Gaussian-variable-reflectivity unstable resonator simply by making the ZnSe window-coupler into a Gaussian-variable-reflectivity output coupler.

# CHAPTER 6

## Data and Results

Data were collected in order to characterize the unobscured unstable resonator design. Recordings were made of the near and far-field beam profiles, the focused spot size and the divergence of the beam after propagation. The near and far-field beam profiles were studied using a pyroelectric vidicom camera. The far-field beam profiles and focused spot sizes were studied by focusing the near-field beam using a 150-cm ZnSe lens. Figure 6.1 illustrates how both the near and far-field beam profiles were recorded.

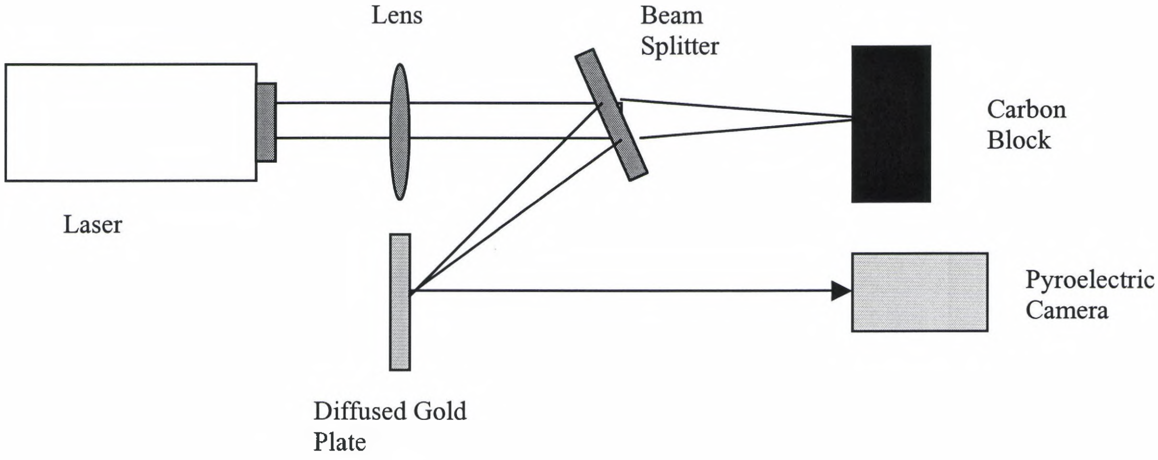

**Figure 6.1**. Set up for recording the near and far-field beam profiles. The lens was removed when recording the near-field beam profile.

In Figure 6.1, a beam splitter was inserted immediately after the 150-cm lens so that only a small percentage (~ 2%) of the focusing beam was focused onto a diffused gold plate, while the rest of the 98% of the beam was dumped onto a carbon block. The pyroelectric camera recorded the beam profile from the heat collected by the diffused plate. The focused spot size was measured by removing the carbon block and placing a plexiglas target at that same location. To record the near-field pattern, the same set up for recording the far-field beam profile was used except the 150-cm lens was removed. The divergence was determined using Plexiglas targets by allowing the beam to propagate to two different locations. The divergence was calculated by taking the ratio of the difference of each target radius to the distance between them. Figure 6.2 illustrates the beam divergence measurement.

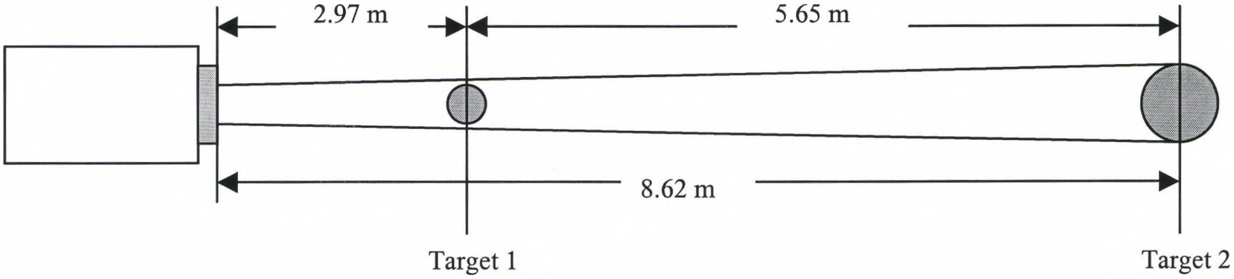

**Figure 6.2**. Illustration on how beam divergence was determined.

In Figure 6.2, the beam exiting the coupler has a radius of 4.25 cm. At Target 1, the burn pattern on the Plexiglas had a radius of 4.38 cm after propagating 2.97 m. Target 2 had a radius of 5.08 cm after propagating 8.62 m. The beam divergence half-angle, $\theta_d$, is given by

$$\theta_d = \frac{(t_2 - t_1)}{d} \quad (6.1)$$

where $t_1$ and $t_2$ are the radii of the burn patterns on Targets 1 and 2, respectively. From Eq. (6.1), the beam divergence half-angle is 1.2 mrad for a distance, d, of 5.65 m between the targets. From the coupler to Target 2, $\theta_d$ is approximately 1 mrad.

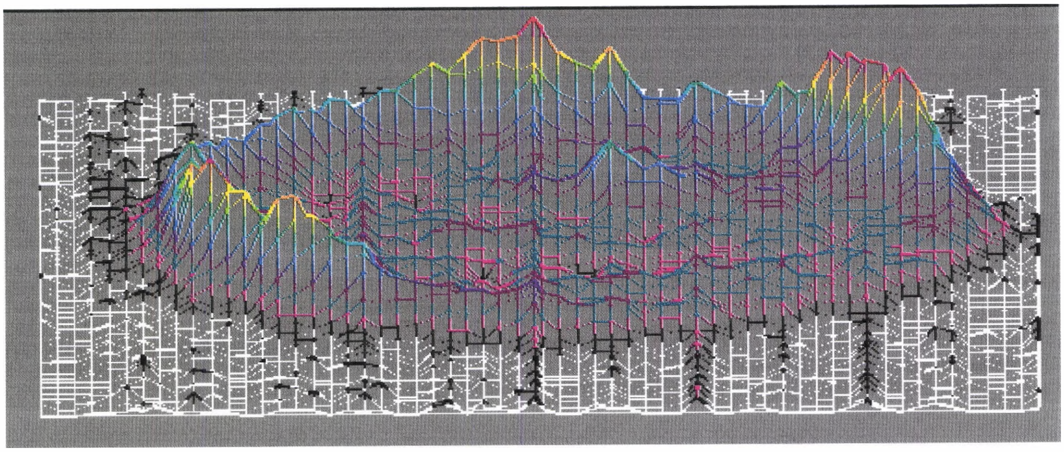

**Figure 6.3 (a)**. 3-D plot of the unfocused beam.

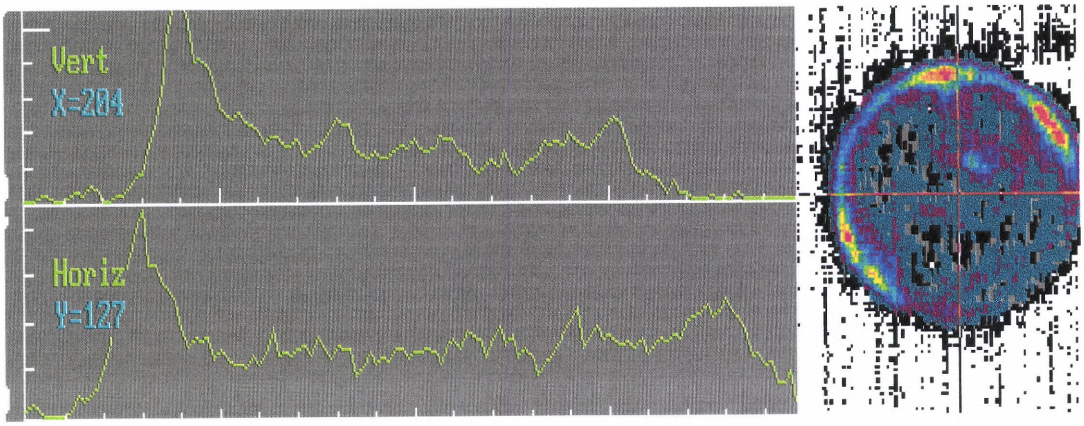

**Figure 6.3 (b)**. Profile of the unfocused beam.

Figures 6.3 (a) and (b) are of the unfocused beam. These Figures illustrate that the resonator is not aligned since the profiles are not symmetric. An output power was measured at approximately 4.7 kW. This is 1.3 kW less than the predicted output power. The difference in output powers is, for the most part, due to the misalignment of the optics. The near-field or unfocused beam, in Figures 6.3 (a) and (b), is very similar to the predicted computer model in Figure 4.5 (a), ignoring the non-symmetry. However, the far-field or focused beam, in Figures 6.3 (c) and (d), is not similar to the single-lobe (quasi-Gaussian) beam in Figure 4.5 (b). In fact, the beam profile Figure 6.3 (c) appears to be the demagnification of the near-field beam profile, and not the transformation from the Fresnel region to the Fraunhofer region. Figures 6.3 (c) and (d) indicate that modes higher than the lowest-order transverse mode are operating in the resonator since the focus is not a "tight" Gaussian spot. Because the resonator is not perfectly aligned, it is coming in contact with the cavity walls of the laser cavity, therefore, creating soft aperture effects. Better or perfect alignment should eliminate these soft aperture effects and allow the lowest-order transverse mode operation and a Gaussian spot at the focus.

Table 6.1 represents an attempt to locate the best (minimum) spot size by adjusting the focusing element back and forth through the focus. Table 6.1 indicates that the smallest spot (in diameter) is 7.5 ± 2 mm. There is an uncertainty of approximately 0.5 mm when using a steel ruler to measure the spot diameter and approximately an 1.5-mm uncertainty in the laser burn consistency on the Plexiglas target, which gives a total uncertainty of 27 %.

**Table 6.1.** Diameter of the burn pattern on the Plexiglas target as a function of position of the 150-cm focal length lens.

| Lens Position (cm) | Burn Spot Diameter (± 2 mm) | Lens Position (cm) | Burn Spot Diameter (± 2 mm) |
|---|---|---|---|
| 140 | 10.0 | 150 | 8 |
| 141 | 10.0 | 151 | 7.5 |
| 142 | 9 | 152 | 8 |
| 143 | 8.5 | 153 | 8.5 |
| 144 | 8.5 | 154 | 9 |
| 145 | 8 | 155 | 9 |
| 146 | 8 | 156 | 9.5 |
| 147 | 7.5 | 157 | 9.5 |
| 148 | 8.5 | 158 | 10.0 |
| 149 | 8 | | |

With this current "best" alignment, 7.5-mm (± 2 mm) is the smallest spot size achieved, which is roughly ten times larger than expected. In addition, the output power is lower than expected. In the attempt to account for the large spot size and the loss of output power, it was realized that this unobscured unstable resonator is employing the entire laser cavity (the full 4-inch diameter). Thus, the resonator becomes extremely difficult to align because the optics must be *perfectly* aligned with each other *and* the cavity in order to keep the internal beam from coming in contact with walls of the laser cavity. To resolve this flaw, a *hard* aperture was designed to actually make the internal propagating beam smaller, which creates more space between the cavity walls and the beam, thus allowing for better alignment. The cathode plate (at the center of the laser cavity) is currently a copper plate with a 4-inch hole in the center. A new cathode plate was designed, with a slightly smaller hole, to act as a hard aperture.

Because the annular mirror does not have a lot of surface area, the size of the hard aperture could only be slightly smaller than the 4-inch diameter hole in the current cathode plate, otherwise too much of an output power loss would occur. In order to determine what size to make the hard aperture, the amount of power loss due to decreased number of passes needed to be determined. To do so, the saturated gain and intensity for the first ten or so passes were derived using the saturation law previously stated in Appendix A

$$\frac{1}{I_i}\cdot\frac{dI_i}{dz}=\frac{\gamma_o}{1+g(\nu)\cdot\dfrac{I_\nu}{I_s}}.$$

Integrating both sides of this equation from, $I_1$ (input intensity) to $I_2$ (output intensity), and from 0 to $l_g$ it can be expressed in the form

$$\ln\left(\frac{I_2}{I_1}\right)+\frac{I_2-I_1}{I_s}=\gamma\cdot l_g \quad . \tag{6. 2}$$

The gain of an homogeneous laser medium will saturate according to[4]

$$\gamma=\frac{\gamma_o}{\left(1+\dfrac{I_\nu}{I_s}\right)}. \tag{6. 3}$$

Thus, by using Eqs. (6.2) and (6.3) the number of passes made through the gain medium until saturation occurs can be calculated. The starting and ending points are needed. The starting point is when $I_\nu$ goes to zero, then $\gamma=\gamma_o$ in Eq. (6.3). The ending point is the limit when $I_v = I_s$. Then Eq. (6.3) becomes $\gamma_n = \gamma_o/2$. Knowing the starting and ending points, and by using Eqs. (6.2) and (6.3) an iterative process can be performed. Starting backwards, we know that when the gain medium is saturated, the maximum intensity will be approximately 134 W/cm$^2$, and the small signal gain coefficient will become 0.0033 cm$^{-1}$ (using the average value of $\gamma_o$ from Table 3.6).

The *ending* values (working backwards) for $\gamma_o/2 = 0.0033$ cm$^{-1}$ and $I_s = 134$ W/cm$^2$ are used, in both Eqs. (6.2) and (6.3), to solve for the intensity, $I_{n-1}$, and the saturated gain coefficient, $\gamma_{n-1,}$ which represent the n-1 pass before the gain medium is saturated. By letting $\gamma_n = \gamma_o/2$, when $I_n = I_v = I_s$ for the nth pass through the gain medium $I_{n-1}$ and $\gamma_{n-1}$ can be determined by using the same procedure as in Chapter 3, Section 3.1, with Eqs. (6.2) and (6.3). For the next iteration, the new values for $I_{n-1}$ and $\gamma_{n-1}$ now become $I_n$ and $\gamma_n$, respectively, and are then substituted into Eqs. (6.1) and (6.2). This iterative process will continue until the "top" of the curve shown in Figure 6.4 reaches 0.0066 cm$^{-1}$. Figure 6.4 is a plot of saturated gain verses output intensity for the values found using the iterative process described above. Using the area of the output beam, 56.75 cm$^2$, the output power can be found using the intensities in Figure 6.4. The output power can then be plotted against the number of passes made.

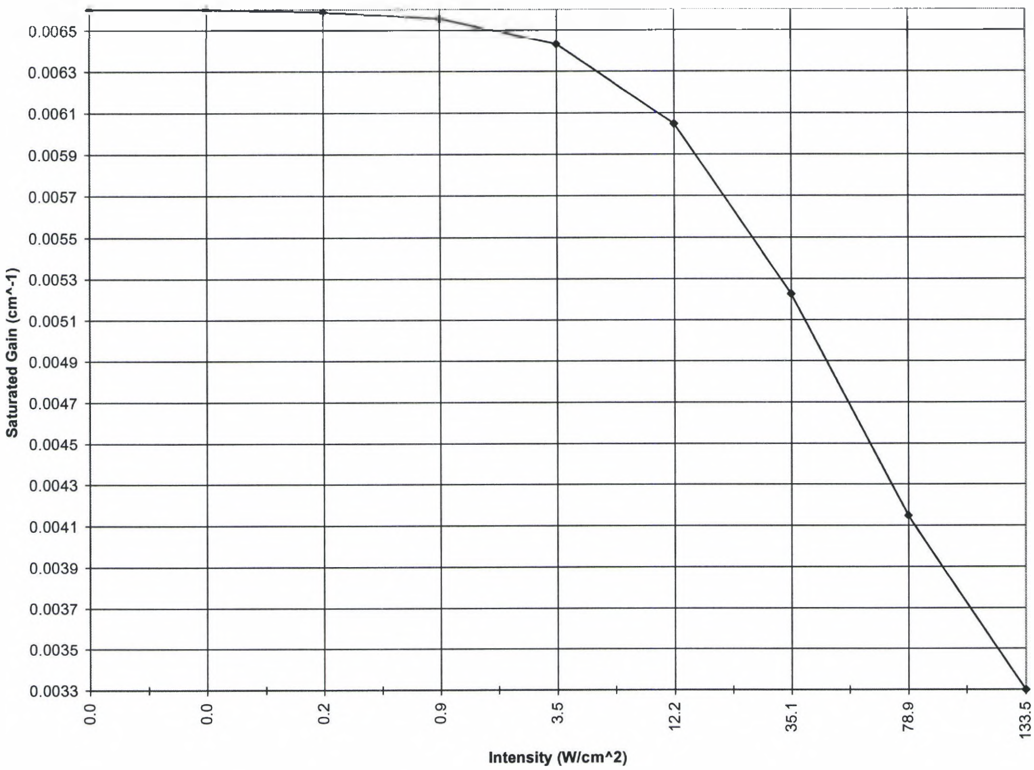

**Figure 6.4.** Saturated gain verses normalized intensity for a homogeneous laser gain medium.

Figure 6.5 shows that the output power drops very quickly; within 3 passes the output power drops 4.5 kW. Therefore, the new cathode plate (hard aperture) was made so that it "cut out" only a very small amount of the beam. In Chapter 4, a 1 mm offset was used as the height for the initial beam in the ray trace. Therefore, the new cathode plate was made to "cut out" 1 mm of the beam, which should still have an output of approximately 6.0 kW when perfectly aligned. This design makes the beam inside the cavity 1 mm smaller, or the cavity wall 1 mm larger.

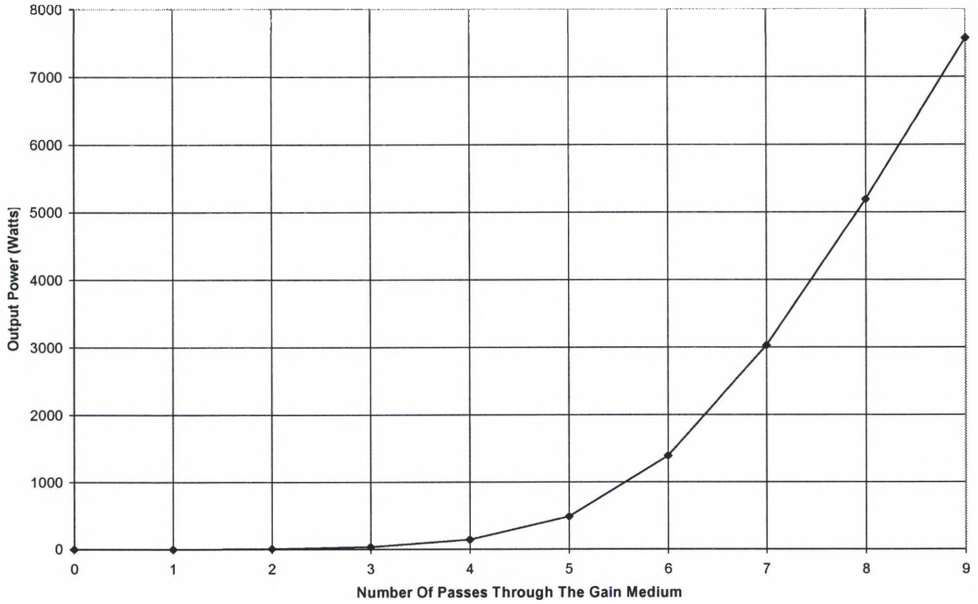

**Figure 6.5**. Output power verses the number of passes made until staturation is reached.

The new cathode plate needed to reflect 1 mm of the unwanted beam away at some angle so that the glass cavity wall would not sustain any damage. The cathode plate was, therefore, designed with a wedge to reflect the radiation away from the cavity walls. Figure 6.6 demonstrates how the light is reflected from the new cathode plate *insert*.

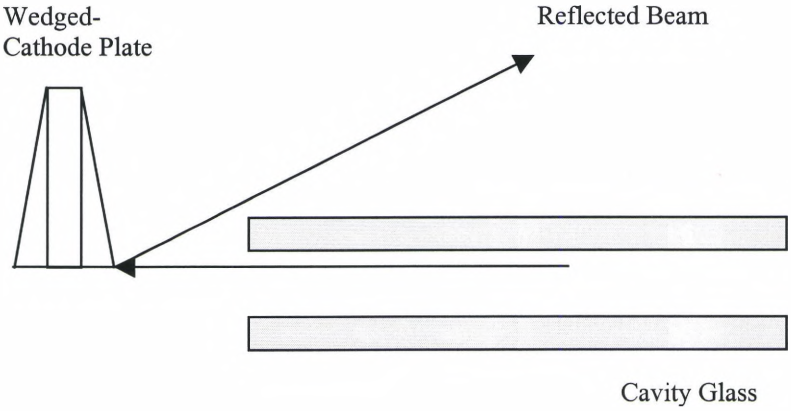

**Figure 6.6**. New cathode plate *insert* demonstrating how the reflected-beam is deflected from the cavity glass walls.

In Figure 6.6, shows the *insert* of the new cathode plate. An insert is used in case 1 mm is not a sufficient amount of space between the beam and the cavity wall for proper alignment. The insert is in the form of an annular ring. The width of the ring is 5.18 cm, which is used to define the angle of the wedge. The inner diameter (I.D.) of the insert is 10.06 cm. The outer diameter (O.D.) is 15.24 cm, which is shown in Figure 6.7.

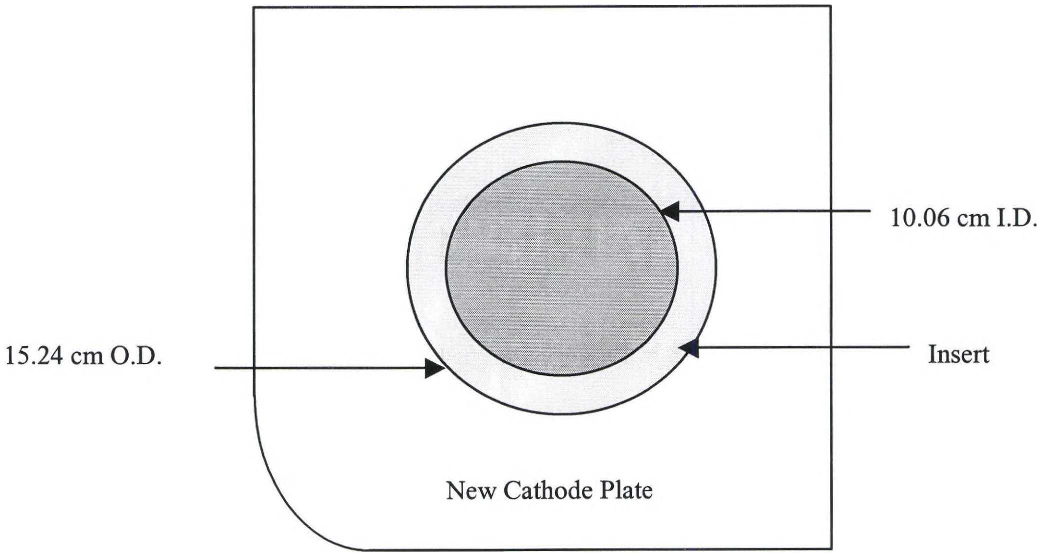

**Figure 6.7**. New cathode plate with insert.

The 1-mm portion of the beam will reflect off of the 13.8-degree wedge at 27.5 degrees (twice the wedge angle – law of reflection) and clearing the glass cavity wall. Again, if 1 mm is not adequate then a larger insert can be made with a smaller I.D., but with the same O.D.

Figures 6.8 (a) through (d) give the unfocused and focused beam profiles with the new cathode plate using the pyroelectric vidicom camera.

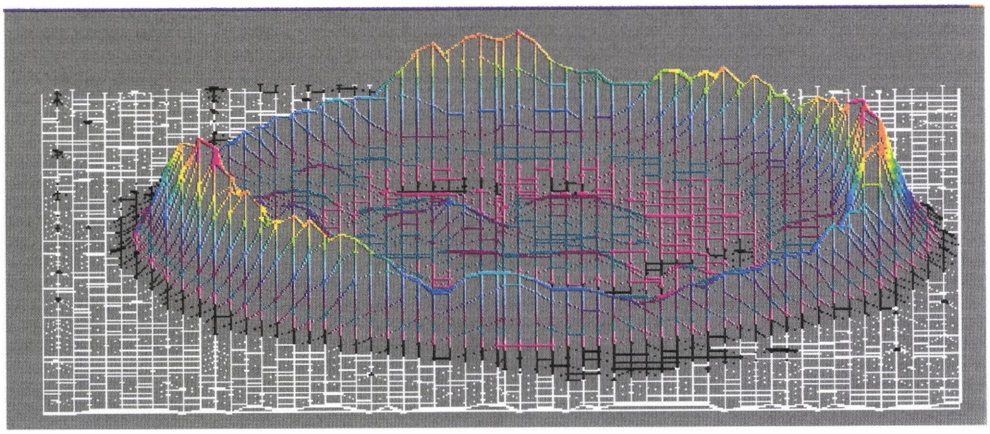

**Figure 6.8 (a)**. 3-D plot of the unfocused beam with the new cathode plate and insert.

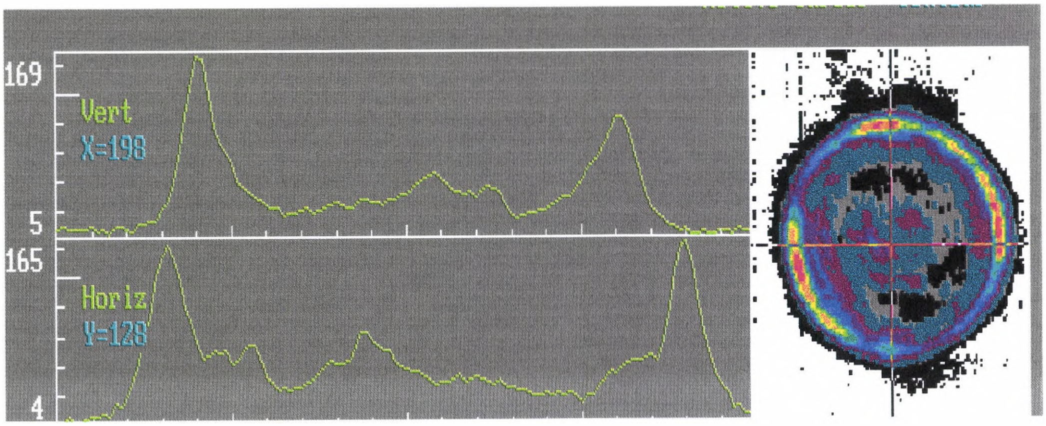

**Figure 6.8 (b)**. Profile of the unfocused beam with the new cathode plate and insert.

When comparing Figures 6.4 with 6.8, before and after the new cathode plate insert, it is fairly obvious that a better alignment was obtained, but the alignment still needs more improvement. Table 6.2 indicates the smallest spot diameter using the new cathode plate.

**Table 6.2**. Diameter of burn pattern on Plexiglas target with the new cathode plate.

| Lens Position (cm) | Burn Spot Diameter (± 2 mm) | Lens Position (cm) | Burn Spot Diameter (± 2 mm) |
|---|---|---|---|
| 145 | 9.5 | 151 | 6.5 |
| 146 | 8.5 | 152 | 7.5 |
| 147 | 8 | 153 | 7.5 |
| 148 | 7 | 154 | 8 |
| 149 | 6.5 | 155 | 8 |
| 150 | 5 | 156 | 8.5 |

In Table 6.2, the spot diameter is smaller (5 mm) with the new cathode plate and insert and the unfocused and focused beam profiles in Figure 6.8 are more symmetric, which suggest that the alignment has improved. The output power extracted from the resonator with the new cathode plate was less than the output power extracted using the original cathode plate. It was measured using the UDBC at approximately 4.5 kW, whereas before it was measured at approximately 4.7 kW. The 1-mm insert is very small, but the ray trace in Chapter 4 shows that five round-trips are made with an initial beam height of 1 mm for perfect alignment. Now considering the 1 mm from the new cathode plate is weighed with the existing imperfect alignment (say 1-mm), this might make a total of two or more millimeters for the initial beam height instead of 1 mm as previously stated for the ray trace. If the initial height is indeed a total of 2 mm, then this corresponds to four round-trips instead of five. Four round-trips can then be thought of as eight complete passes through the gain medium and in Figure 6.5, after eight passes the total output power is calculated to be approximately 5,200 W. This more closely matches the experimental data of 4,500 to 4,700 W.

The alignment using the new cathode plate may have given slightly better alignment, but a 1-mm smaller cavity is not adequate. A larger insert should and can be designed for the existing cathode plate. The data obtained from a larger insert will solve the alignment issue and, in addition, help support the preceding data. However, significant output power will be sacrificed. Another option, although more expensive, may be to re-manufacture the optics to make them smaller diameters to allow for a larger cavity. There is still confidence that this resonator, with proper alignment, will produce very small spot diameters, thus generate an extremely intense Gaussian-type focused beam profile.

# APPENDIX A

## Rigrod Equation Derivation

The output irradiance can be derived using the saturation law written as[2]

$$\frac{1}{I_i}\cdot\frac{dI_i}{dz}=\frac{\gamma_o}{1+g(\nu)\cdot\dfrac{I_\nu}{I_s}}.$$

where $I_i$ is the one-way flux in the given direction and $I_\nu$ is the total flux at a position "z" in all directions. We are only concerned with radiation close to line center where[2]

$$g(\nu)=1.$$

The saturation law then becomes

$$\frac{1}{I_i}\cdot\frac{dI_i}{dz}=\frac{\gamma_o}{1+\dfrac{\Sigma I_i}{I_s}}.$$

Now after separating the variables

$$\frac{dI_i}{I_i}\cdot\left(1+\frac{\Sigma I_i}{I_s}\right)=\gamma_o dz.$$

To be accurate the left-going intensities ($I_1$ & $I_2$) originate from mirror, $M_2$, and propagate towards the mirror, $M_1$. Likewise the right-going intensities ($I_3$ & $I_4$) originate at $M_1$ and travel towards $M_2$. Figure A.2 depicts this process.

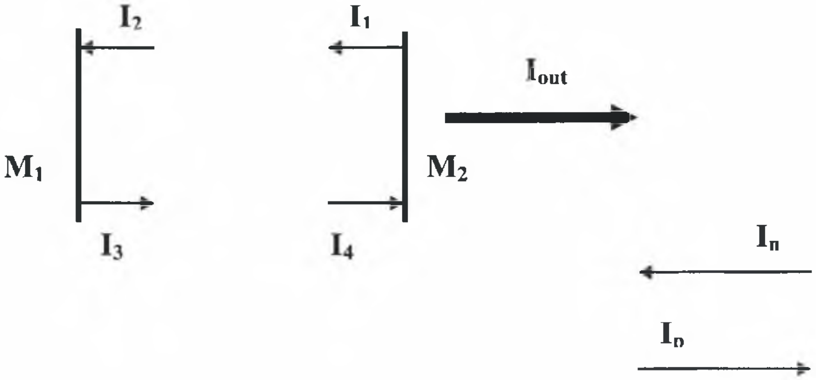

**Figure A.2.** $I_1$ & $I_2$ are the left-going intensities towards the back mirror, $M_1$.
$I_3$ & $I_4$ are the right-going intensities towards the front mirror, $M_2$.

In Figure A.2, since $I_1$ & $I_3$ both leave mirrors, $M_1$ & $M_2$, they can be defined as

$$I_1 = I_4 \cdot (1 - L_m - L_c),$$

and

$$I_3 = I_2 \cdot (1 - L_m).$$

Where $L_m$ is the mirror loss ($L_m$ is approximately equal to 0.02), and $L_c$ is the output coupling losses from $M_2$.

Referring back to the separate variable saturation law equation again

$$\frac{dI_v}{I_v} \cdot \left(1 + \frac{I_v}{I_s}\right) = dz \cdot \gamma_o,$$

we see that for the positive (right-going) direction it becomes

$$\frac{dI_i}{I_i}\cdot\left(1+\frac{\Sigma I_i}{I_s}\right)=\gamma_o dz$$
,

where $I_p$ & $I_n$ are the left- and right-going intensities respectively. The right-going equation can be simplified

$$\frac{dI_p}{I_p}\cdot\left(1+\left(\frac{I_p}{I_s}+\frac{K}{I_p\cdot I_s}\right)\right)=z\cdot\gamma_o,$$

where $K = I_p I_n$. Now, integrating over $I_3$ & $I_4$ for the positive direction:

$$\int_{I_3}^{I_4}\frac{1}{I_p}\cdot dI_p+\frac{1}{I_s}\cdot\int_{I_3}^{I_4}\frac{I_p}{I_p}\cdot dI_p+\frac{K}{I_s}\cdot\int_{I_3}^{I_4}\frac{1}{I_p}\cdot dI_p=\gamma_o\cdot\int_{I_3}^{I_4}1\cdot dI_p\,.$$

After integration we have

$$\ln\left(\frac{I_4}{I_3}\right)+\frac{1}{I_s}\cdot(I_4-I_3)+\frac{K}{I_s}\cdot\left(\frac{1}{I_4}-\frac{1}{I_3}\right)=\gamma_o\cdot\lg\,.$$

Similarly, in the negative direction:

$$\ln\left(\frac{I_2}{I_1}\right)+\frac{1}{I_s}\cdot(I_2-I_1)+\frac{K}{I_s}\cdot\left(\frac{1}{I_2}-\frac{1}{I_1}\right)=\gamma_o\cdot\lg\,.$$

Next, add both positive and negative equations together to get

$$\ln\left(\frac{I_4}{I_3}\cdot\frac{I_2}{I_1}\right)=termA\,,$$

$$\left(\frac{I_4-I_3}{I_s}\right)+\left(\frac{I_2-I_1}{I_s}\right)=\frac{(I_4-I_3)+(I_2-I_1)}{I_s}=termB\,,$$

and

$$\frac{K}{I_s}\cdot\left[\left(\frac{1}{I_4}-\frac{1}{I_3}\right)+\left(\frac{1}{I_2}-\frac{1}{I_1}\right)\right]=termC\,.$$

Simplifying term C:

$$\frac{K}{I_s}\cdot\left(\frac{1}{I_4}-\frac{1}{I_3}\right)+\frac{K}{I_S}\left(\frac{1}{I_2}-\frac{1}{I_1}\right)=\left(\frac{1}{I_4}-\frac{1}{I_1}\right)+\frac{K}{I_S}\left(\frac{1}{I_2}-\frac{1}{I_3}\right)=\frac{1}{I_S}\cdot\left(I_1-I_4+I_3-I_2\right),$$

where K = $I_1$ $I_4$ = $I_2$ $I_3$. Thus, term B = term C. Therefore,

$$\ln\left(\frac{I_4}{I_3}\cdot\frac{I_2}{I_1}\right)+2\cdot\left[\frac{1}{I_s}\cdot\left(I_1-I_4+I_3-I_2\right)\right]=2\cdot\gamma_O\cdot\mathrm{lg}.$$

Now substituting

$$I_1=I_4\cdot\left(1-L_m-L_c\right),$$

and

$$I_3=I_2\cdot\left(1-L_m\right),$$

into terms B & C we get

$$\left(\frac{2}{I_S}\right)\cdot\left[I_4\cdot\left(L_m+L_c\right)+I_2\cdot L_m\right]=termsB\&C.$$

Now solve for $I_2$ in terms of $I_4$:

$$K=I_1\cdot I_1=I_4\cdot\left[I_4\cdot\left(1-L_m-L_c\right)\right],$$

and

$$K=I_2\cdot I_3=I_2\cdot\left[I_2\cdot\left(1-L_m\right)\right].$$

Therefore,

$$K=\left(I_4\right)^2\cdot\left(1-L_m-L_c\right)=\left(I_2\right)^2\cdot\left(1-L_m\right),$$

and $I_2$ then becomes

$$I_2=I_4\cdot\sqrt{\frac{\left(1-L_m-L_c\right)}{\left(1-L_m\right)}}.$$

Now terms B & C become

$$\frac{2\cdot I_4}{I_s}\cdot\left[\left(L_m+L_c\right)+L_m\cdot\sqrt{\frac{\left(1-L_m-L_c\right)}{\left(1-L_m\right)}}\right]=termsB\&C.$$

Term A now becomes

$$\ln\left(\frac{I_4}{I_3}\cdot\frac{I_2}{I_1}\right)=\ln\left[\frac{1}{(1-L_m)}\cdot\frac{1}{(1-L_m-L_c)}\right].$$

Now add simplified terms B & C and subtract term A over to the 2γolg side:

$$\frac{2\cdot I_4}{I_s}\cdot\left[(L_m+L_c)+L_m\cdot\sqrt{\frac{(1-L_m-L_c)}{(1-L_m)}}\right]=2\cdot\gamma_o\,\mathrm{lg}+\ln\left[(1-L_m)\cdot(1-L_m-L_c)\right],$$

and $I_4$ is equal to $\frac{I_{out}}{L_c}$, therefore

$$\frac{I_{out}}{I_s}=\frac{L_c}{2}\left[\frac{2\gamma_o l_g+\ln\{(1-L_m)(1-L_m-L_c)\}}{\left[(L_m+L_c)+L_m\sqrt{\frac{(1-L_m-L_c)}{(1-L_m)}}\right]}\right]$$

This result, $I_{out}/I_s$, can also be written as[2]

$$\frac{I_{out}}{I_s}=\frac{t_b t_2\left[\gamma_o l_g-\frac{1}{2}\ln\left(\frac{1}{t_a{}^2 t_b{}^2 r_1 r_2}\right)\right]}{\left(1-\sqrt{t_a{}^2 t_b{}^2 r_1 r_2}\right)\left(1+\sqrt{\frac{r_2 t_b{}^2}{r_1 t_a{}^2}}\right)}$$

# APPENDIX B

## Spot Size and Output Beam Diameter for LHMEL I-T

The spot size and output beam diameters were theoretically calculated for the LHMEL facility's laser system (LHMEL I-T) which employs a stable resonator. The output beam diameter is dependent on the multi-mode beam waist radius given by[14]

$$\omega = \omega_o \mathrm{N}^{\frac{1}{2}} \quad . \tag{B- 1}$$

Here N is the Fresnel number and $w_o$ is the spot size of the stable resonator. The spot size is defined as[14]

$$w_o = \left( \frac{\lambda \cdot \mathrm{L}_{\mathrm{cav}}}{\pi} \right)^{0.5} \left[ \frac{1 - \frac{L_{cav}}{R_1}}{\frac{L_{cav}}{R_1}} \right]^{0.25} \quad . \tag{B- 2}$$

Here $L_{cav}$ is the length of the cavity (350-cm) and $R_1$ is the radius of curvature of the back mirror (3,500-cm). From these values the spot size is calculated to be 0.57 cm, and the beam radius is therefore found to be 4.945 cm. Thus, the beam diameter of the stable resonator is 9.889 cm.

# APPENDIX C

## Plots For The $I_s$ And $\gamma_o$ Experiments

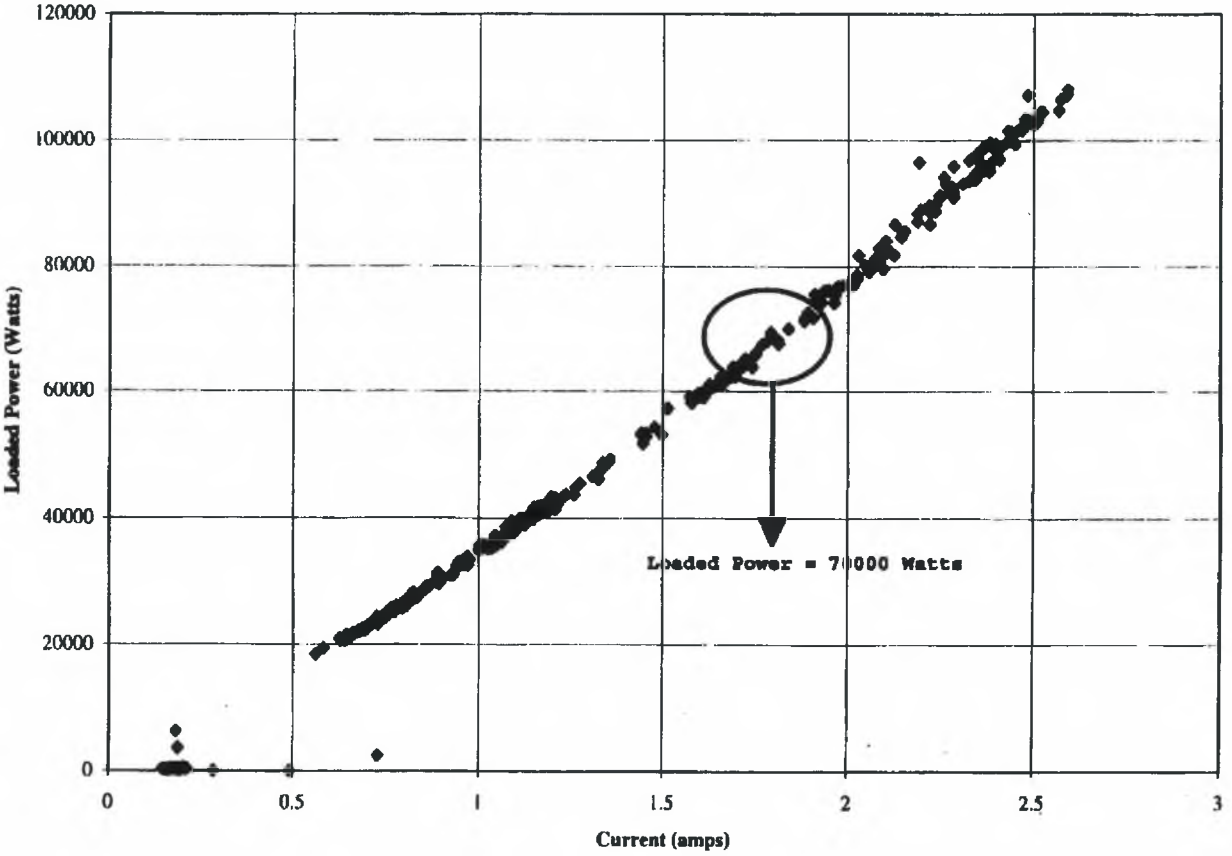

**Figure C-1.** Plot of loaded power verses current for the 75% coupler.

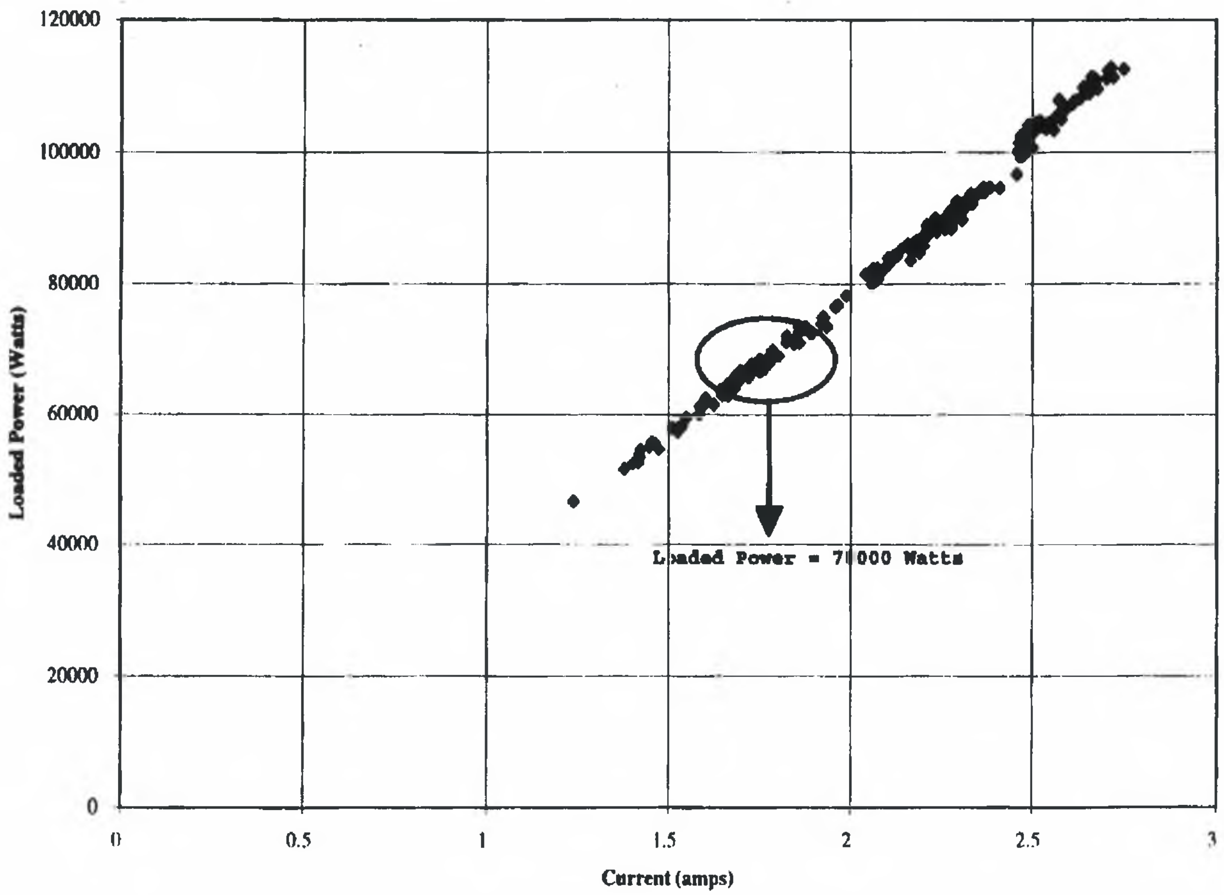

**Figure C-2**. Plot of loaded power verses current for the 60% coupler.

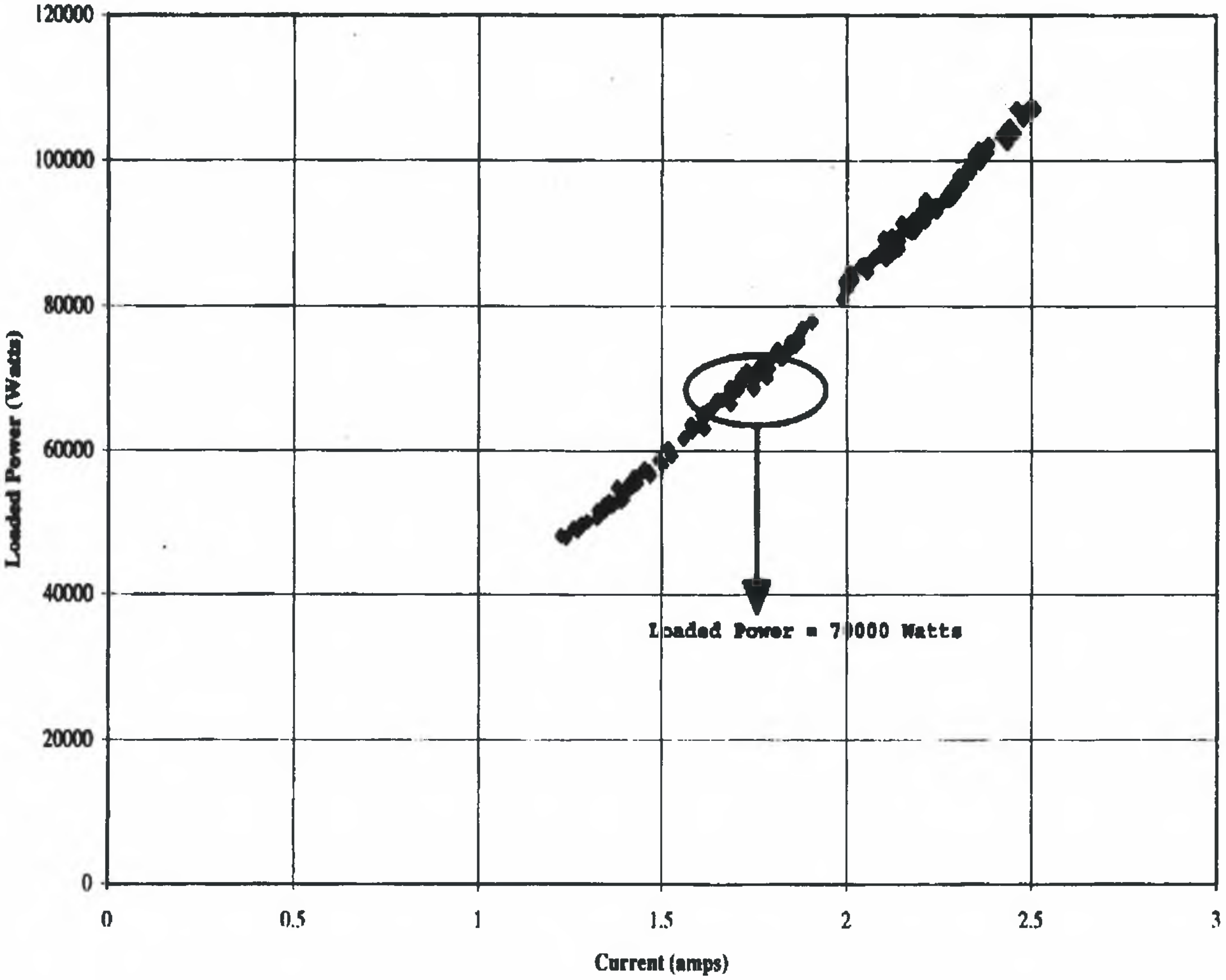

**Figure C-3**. Plot of loaded power verses current for the 17% coupler.

# APPENDIX D

## $CO_2$ Gain Medium

The LHMEL I-R laser gain medium consists of $CO_2$ gas that is mixed with $N_2$ and He (1:5:30) at 49-52 Torr, and is assumed to be homogeneous since it falls within the collision-broadened regime. According to Figure D-1, the absorption coefficient increases linearly with the number of molecules at lower $CO_2$ pressures (Doppler-broadened), but as the $CO_2$ pressure increases above 5.2 Torr the absorption coefficient becomes independent of pressure (collision-broadened).

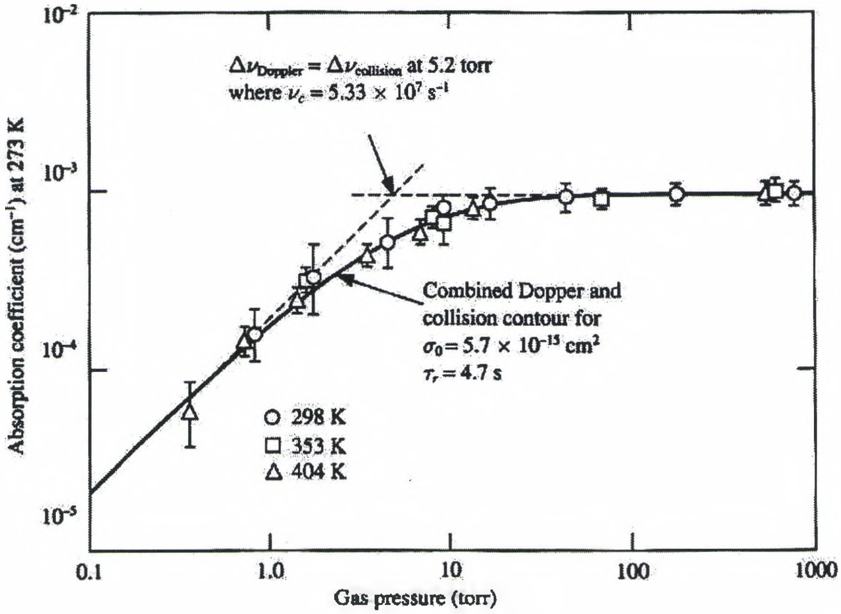

**Figure D-1:** Absorption coefficient of $CO_2$ gas for the 10.6-μm $CO_2$ laser as a function of $CO_2$ pressure. [Reference No. 17.]

In Figure D-1, at 5.2 Torr and where $\nu_c$ is 53 MHz, the Doppler-broadened line width and the collision-broadened line width are equal. Beyond 53 MHz, when the $CO_2$ pressure is greater than 5.2 Torr, the $CO_2$ gain medium is in the collision-broadened region. The collision frequency for LHMEL I-R, $\nu_{LHMEL}$, was calculated by[4]

$$\nu_{LHMEL} = N_m \sigma \left[ \frac{8kT}{\pi} \left( \frac{1}{M_m} + \frac{1}{M_n} \right) \right]^{\frac{1}{2}} , \qquad \text{(D- 1)}$$

where k is Boltsman's constant, T is the temperature in Kelvins, $\sigma$ is the cross sectional area for the $CO_2$ molecule ($5.7 \times 10^{-15}$ $cm^2$) and M are the masses of the colliding atoms of type m and n. $N_m$ is the density of the projectiles and is given by[6]

$$N_m = \frac{P}{kT} , \qquad \text{(D- 2)}$$

where P is the pressure of the $CO_2$ gas. Therefore, at 50 Torr and approximately 400 degrees K the collision frequency for LHMEL I-R $CO_2$ molecules was calculated

$$\nu_{LHMEL} = 5.2 \text{ x } 10^8 \text{ s}^{-1} .$$

This corresponds to a density of projectiles, Eq. (D-2), in the LHMEL I-R laser medium of

$$N_{mLHMEL} = 1.8 \text{ x } 10^{18} \text{ atoms / cm}^3 .$$

The LHMEL I-R laser medium has a high collision frequency and is operating at a high $CO_2$ pressure, which, according to Figure D-1, means that the absorption coefficient of the 10.6-μm radiation by $CO_2$ is independent of pressure. This supports the assumption that the LHMEL I-R $CO_2$ laser medium is operating in the collision-broadening regime, therefore is considered to be homogeneous.

# APPENDIX E

## Alignment Procedure

The unobscured unstable resonator optics (toric and annular mirrors and the ZnSe window) were mounted into the LHMEL I research laser. The optical fixtures used for the unstable resonator optics were designed to adapt to the three-point alignment mount previously used for LHMEL I-R (see Figure E.1).

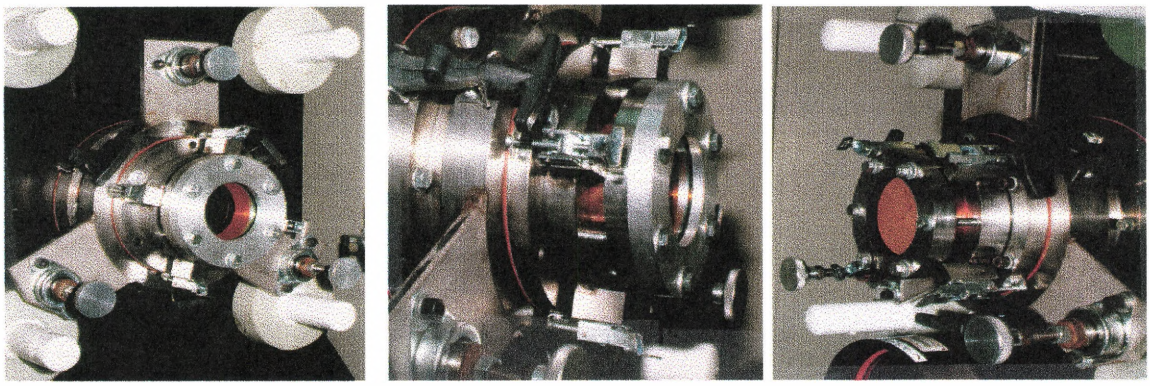

(a) (b) (c)

**Figure E.1**. (a) Front view of coupler; (b) side view of coupler; (c) view of back toric mirror.

Figure E.1 (a) shows how the ZnSe window and annular mirror are seated together. The annular mirror is first placed in an aluminum fixture setting on a rubber gasket. Then another aluminum fixture is placed on the backside of the annular mirror with a gasket to seal that surface. The ZnSe window is then placed on the backside of the annular mirror, in the same aluminum fixture, with a rubber gasket sandwiched in between the two. Then

In Figure E.2 the HeNe laser propagates through the ZnSe window to the back toric mirror where it reflects off of the toric mirror and diverges as it propagates back to the coupler. Therefore, a larger HeNe beam diameter will create a larger toric ring. The HeNe spot in the center of toric ring is from the initial beam propagating through the ZnSe window. The inner diameter of the toric ring remains constant, this is caused from the HeNe rays hitting the back toric mirror directly on center. The back toric mirror resembles a cone when viewing it from the front, therefore, when the HeNe spot is aligned with the back mirror it will form a *uniform* ring (toric ring). In other words, the ring should have the same thickness 360 degrees around. If the HeNe is off center in relation to the back mirror this will be evident by observing a non-uniform toric ring. Figure E.3 demonstrates a HeNe beam that is not aligned to the back mirror.

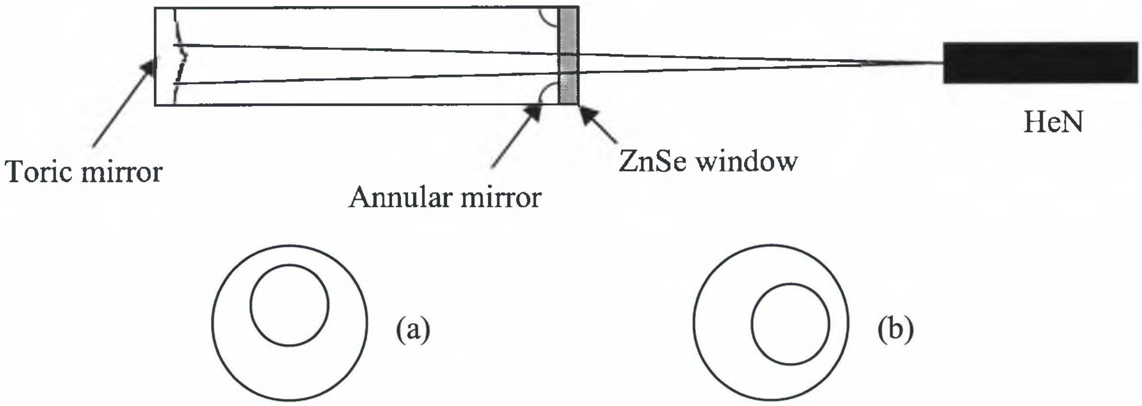

**Figure E.3**. An example of a HeNe beam that is not aligned.
(a) HeNe beam is not vertically aligned.
(b) HeNe beam is not horizontally aligned.

Compare Figure E.2 with Figure E.3 (a) and (b). It is evident that the HeNe beam in Figure E.2 is properly aligned to the back toric mirror, whereas in Figure E.3 (a) and (b) the HeNe are not aligned.

The system is best aligned by using the following **five** steps. **1)** Align the HeNe laser to the cavity with both the coupler and the back target. *Note: the HeNe must be aligned with the ZnSe window so that the system will be aligned to the optical axis.* The back target is placed into the same mount where the toric mirror would be, and an 8.5-cm target onto the cover plate in front of the ZnSe window. Apply the vacuum so that both the coupler and the back target are held in place. The coupler can now be aligned under vacuum. **2)** Align the coupler – adjust the coupler vertically to the calculated reflection spot, then laterally using a course adjustment. *Note: the calculated reflection spot will be discussed later.* **3)** Shut off the vacuum and replace the back target with the back toric mirror. Apply the vacuum again, and now make sure the "toric" ring is uniform (it is ok if it is not centered). If it is not uniform repeat steps one through three until it is uniform. **4)** Adjust the back toric mirror to center it on the 8.5-cm target (the 8.5-cm target should have a grid with cross hairs and small hole in the center). **5)** Make the first shot onto plexiglas, and start the iteration process. *Note: the iteration process will be discussed later, and it is important that these steps be followed in sequence for proper alignment.*

The *calculated reflection spot* is determined from the HeNe reflecting off of the ZnSe window which is at a 1.5-degree ***vertical*** tilt. The tilt is from a 1.5-degree wedge on the backside of the annular mirror that the flat/flat ZnSe window lies on. The 1.5-degree tilt in the ZnSe window prohibits any parasitic lasing to occur. The tilt will cause the HeNe beam to reflect off of the ZnSe window and head back towards aligning mirror at optimized, then some *minor* adjustments can be made. Figure E.5 and Table E.1 illustrates the iterative process of aligning the resonator.

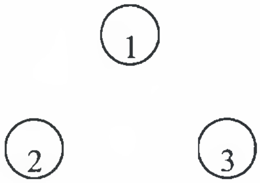

**Figure E.5**. Front view of the optic adjusting knobs (front coupler & back mirror).

In Figure E.5, knob #1 is for vertical adjustment only and knobs #2 and #3 are for *lateral* and vertical adjustments. Figure E.5 is used to help understand Table E.1.

**Table E.1**. Ten adjustments were made before best alignment. Each adjustment required one plexiglas burn.

| **Knob 1** | δ | Δ | **Knob 2** | δ | Δ | **Knob 3** | δ | Δ | **Burn #** |
|---|---|---|---|---|---|---|---|---|---|
| ---- | 0 | 0 | ---- | 0 | 0 | ---- | 0 | 0 | 1 |
| ccw | 4mm | 4mm | ---- | 0 | 0 | ---- | 0 | 0 | 2 |
| ccw | 2mm | 6mm | ---- | 0 | 0 | ---- | 0 | 0 | 3 |
| ccw | 1mm | 7mm | ---- | 0 | 0 | ---- | 0 | 0 | 4 |
| ccw | 1mm | 8mm | ---- | 0 | 0 | ---- | 0 | 0 | 5 |
| ccw | 1mm | 9mm | ---- | 0 | 0 | ---- | 0 | 0 | 6 |
| ccw | 1mm | 10mm | ---- | 0 | 0 | ---- | 0 | 0 | 7 |
| ccw | 1mm | 11mm | ---- | 0 | 0 | ---- | 0 | 0 | 8 |
| cw | 1/2mm | 10.5mm | ---- | 0 | 0 | ---- | 0 | 0 | 9 |
| cw | 1/2mm | 10mm | cw | 1/4mm | 1/4mm | ccw | 1/4mm | 1/4mm | 10 |

In Table E.1 the first column (knob 1) is the direction the knob is being turned, clockwise or counter-clockwise. The second column (δ) is the magnitude of the turn. The third column (Δ) is the total magnitude/deviation from *center* (δ = 0mm) that the knob has been turned. The last column is the plexiglas burn (one burn per adjustment). From Table E.1 it is shown that up until burn number ten only vertical adjustments were made. It could have been the other case, where the majority of adjustments were lateral; it just depends on the first burn pattern. If the first burn has a fairly defined edge, but the central region does not show much irradiance then vertical adjustments should be made first. If, on the other hand, there is no defined edge, and it almost looks as if the burn represents a scattered irradiance then lateral adjustments should be made first. By knowing which adjustment to make first (vertical or lateral on the front coupler) *a lot of time will be saved*. Again, the back mirror should *always* be adjusted after the coupler has been optimized, and the same table as Table E.1 should be used to keep track of the adjustments.

# References

1. Eugene Hecht, *Optics, Second Edition* Addison-Wesley Publishing Company, Menlo Park, California, (1987).

2. Hahaa E. A. Saleh, M. C. Teich, *Fundamentals of Photonics* John Wiley and Sons, Inc., New York, (1991).

3. Air Force Institute of Technology School of Engineering Physics Dept. Faculty, *Laser and Optics* Wright-Patterson Air Force Base, Dayton, Ohio.

4. Joseph T. Verdeyen, *Laser Electronics, Third Edition* Prentice Hall, Englewood Cliffs, New Jersey, (1995).

5. Jeff Hecht, *The Laser Guidebook* McGraw-Hill, Inc., New York, (1986).

6. A. E. Siegman, *Lasers* University Science Books, Mill Valley CA, (1986).

7. P. E. Jackson, D. R. Hall, *The Physics and Technology of Laser Resonators* Wiley and Sons, Inc., New York, (1989).

8. Grant R. Foules, *Introduction To Modern Optics* Holt, New York (1975).

9. Janos Technology Inc., Tel. 1800-338-9764.

10. Acurex Corporation, Aerotherm Division, Part No. 04459-00, Tel. 419-961-6100.

11. National Institute for Science and Technology.

12. P. W. Milonni, J. H. Eberly, *Lasers* John Wiley and Sons, Inc., New York, (1988).

13. James Reilly, Northeast Science and Technology, [private communications], 117 North Shore Blvd., East Sandwhich, MA 02538.

14. K. Maxwell, M. Lander, D. Daniels, M. Wolf, D. Seibert, C. Oblinger, J. Bagford, *The Laser Hardened Materials Evaluation Laboratory (LHMEL)*

Materials Directorate, Wright Laboratory, Air Force Material Command, Wright-Patterson Air Force Base, OH 45433-7734.

15. E. F. Yelden, H. J. Seguin, C. E. Capjack, S. K. Nikumb, “A Multi-channel Slot Discharge $CO_2$ Laser Employing A Toric Unstable Resonator,” Optics Communications, Volume 82, number 5, 6 (May 1991).

16. Glad 4.4 Beam Characterization Computer Program.

17. E. T. Gerry, D. A. Leonard, “Measurement of 10.6-μm $CO_2$ Laser Transition Probability and Optical Broadening Cross Sections,” Applied Physics Letters, Volume 8, Number 9, (May 1966).